Modeling suffusion of ideally gap-graded soil

Tanawat Tangjarusritaratorn[1]; Yuusuke Miyazaki[2]; Mamoru Kikumoto[3]; and Kiyoshi Kishida[4];

Abstract: A novel framework for describing suffusion in cohesionless soil, incorporating ideally gap-graded soil, is presented in this paper. The key assumption of the proposed simulation is that an erodible particle flow is induced primarily by drag force. The multiphase flow simulation for seepage–soil particle flow phenomena is conducted based on the proposed framework. The validity of the proposed method is checked through a simulation of past laboratory experiments, in which the variation in grain size distributions is grasped by a sieve analysis. The primary results show cumulative fines loss; therefore, a comparison of the cumulative fines loss is mainly discussed in this research. In addition, a discussion is given on the two different parameters affecting the erosion behavior, namely the $p - value$ in the tortuosity function, $T(\emptyset)$, and the clogging relaxation time, β_{clog}. The tortuosity is the ratio of the actual flow path and the distance between its ends, while clogging relaxation time is the parameter that considers the particle flow through the bottleneck. The results show that the numerical simulation provides a good correlation with the experiment, while the $p - value$ is 3 which is the highest value for a geo-material. Moreover, the simulation results of the cumulative fines loss for each particle size also confirm that smaller particles will be fully eroded earlier than larger ones, and that larger particles will slowly become detached from the soil mass.

Author keywords: Suffusion; Multiphase flow; Drag force; Cohesionless soil; Tortuosity.

[1]Graduate Student, Dept. of Urban Management, Kyoto Univ., Japan (corresponding author), Room 338, C1-2 Bldg., Katsura Campus. Nishikyo-ku, Kyoto, 615-8540, Japan. E-mail: tangjarusritaratorn.tanawat.w16@kyoto-u.jp

[2]Assistant Professor, Dept. of Urban Management, Kyoto Univ., Japan, Room 334, C1-2 Bldg., Katsura Campus. Nishikyo-ku, Kyoto, 615-8540, Japan. E-mail: miyazaki.yusuke.6w@kyoto-u.ac.jp

[3]Associate Professor, Dept. of Urban Innovation, Yokohama National Univ., Japan, Tokiwadai 79-5, Hodagaya Yokohama, Kanagawa, 240-8510, Japan. E-mail: kikumoto-mamoru-fc@ynu.ac.jp

[4]Professor, Dept. of Urban Management, Kyoto Univ., Japan, Room 335, C1-2 Bldg., Katsura Campus. Nishikyo-ku, Kyoto, 615-8540, Japan. E-mail: kishida.kiyoshi.3r@kyoto-u.ac.jp

Introduction

Internal erosion plays a key role in the failure of geo-structures, especially in earth dams [1, 2]. In order to mitigate such erosion, the empirical approach is often used. However, the design applied in this approach cannot very well assure the safety of the structure [3]. Suffusion is one of the internal erosion phenomena in which the fine particles experience detachment, movement, and deposition due to the seepage flow among the coarse particles remaining as a soil skeleton [4, 5, 6, 7].

According to the nature of suffusion, the fine particles, namely, those that are small enough in size to travel through the void spaces, are located in the gaps between the large particles. Hence, suffusion can be mostly observed in gap-graded soil. Attempts have been made in several experiments, using either natural materials or manufactured materials, to clarify suffusion. It has been shown that, when homogeneous materials or the consistency of the experiments is considered, it is better to use glass beads because the inconsistencies of natural sand materials can be avoided through the use of these beads [8]. Similar experiments on suffusion have been conducted with gap-graded soil under an upward flow and isotropic stress [9]. Bendahmane, Marot & Alexis (2008) investigated the factors that influence the suffusion mechanism using a soil mixture of kaolinite and Loire sand, with the kaolinite standing for the erodible particles, by changing the particle size distribution and hydraulic conditions [10]. Furthermore, suffusion tests were conducted not only under isotropic stress, but also with different stress paths [11].

In the series of experiments on suffusion conducted by many researchers, it was empirically discovered that what mattered in controlling the erosion rate was the difference between the hydraulic shear stress and the critical hydraulic shear stress, τ_c. According to the experimental findings, the shear stress-based method, which considers both hydraulic shear stress τ_a and erosion coefficient ω, was adopted in order to establish a continuum-based numerical model. In general, for the soil model representing the erosion behavior in previous research, an additional fraction, representing the erodible particles, was required [12, 13]. Subsequently, the erosion rate, $\dot{\varepsilon}$, and the initiation of erosion, which affect the concentration of erodible particles, were governed together by the general form as a function of hydraulic shear stress τ_a, as shown in **Eq. (1)** [14, 15, 16]. However, two constant variables are required for this function, namely, critical hydraulic shear stress τ_c and erosion coefficient ω, as shown in **Eq. (1)**. They are experimentally obtained for each specific soil.

$$\dot{\varepsilon} = \omega(\tau_a - \tau_c) \tag{1}$$

In addition, some previous studies have made an effort to consider the particle transportation of erodible particles together with the erosion rate, while the particle flow velocity is still replaced by the fluid flow velocity [13, 17, 18]. Nevertheless, an experimental study on sand boiling showed that the particle flow velocity is different from the fluid flow velocity [18]. Additionally, the relative velocity between the particle flow and the fluid flow for sand boiling (piping) was analytically confirmed under the assumption of the microscopic scale [18, 19]. This could imply that the particle flow occurring in porous media during suffusion might not be able to be replaced by the fluid flow velocity

However, **Eq. (1)** relies on τ_c and ω, difficult parameters to accurately define, as well as the unrealistic assumption that the particle flow velocity always equals the fluid flow velocity. Considering the procedure for the numerical simulation, the previous simulation scheme always required an experimental test of erosion which could sometimes be time-consuming. In addition, it is not possible to consider the particle transportation using only **Eq. (1)** itself, owing to the disappearance of the erodible particles from the soil mass. Moreover, the particle transportation is further considered by dividing the erodible fraction into erodible particles and movable particles whose mass exchange rate is governed by **Eq. (1)**. Nevertheless, the replacement of the particle flow velocity by the fluid flow velocity cannot provide sufficient consideration to the particle transportation in terms of the different flow velocities between the fluid and the particle phases. Therefore, a numerical model for suffusion, considering the actual particle flow velocity, might be a preferable method to represent the suffusion mechanism.

Attempts have been made to clarify suffusion with the numerical approach, not only by the continuum method, but also by a meshless method as well. In recent years, the implementation of a DEM (discrete element method) simulation for suffusion behavior has become more favorable as it can better show the results with the microscopic scale of the particle transport. The coupling simulation of DEM-CFD, in which the fluid flow is still simulated by the continuum method, is recently being used to describe the suffusion mechanism, especially in small-scale tests [20, 21]. Moreover, the DEM-LBM has recently been developed for the further investigation of the suffusion behavior such that the high resolution of the fluid flow and the fluid-particle flow interaction could be better illustrated [22]. Nevertheless, some difficulty remains in the scaling up of the simulation due to the calculation method which requires a higher computational cost due to the increase in the number of distinct particles.

Considering the previous research works, the aim of the present research is to suggest a new numerical method which can be considered as an intermediary method between the continuum approach, in which the original suffusion concept and a shear-stress based method are used, and a meshless approach, such as the discrete element method. This numerical simulation is still based on the continuum method in order to keep the advantage of lower computational cost

consumption, while the domain is scaled up. In addition, the drawback of the conventional suffusion model, in terms of particle transportation, can be managed with the newly proposed method. In order to cope with the particle flow velocity that depends on the different grain sizes, a multiphase flow simulation is used to consider the different sizes of the particle flow. This numerical method becomes a more generalized model, created as a result of taking the grain size distribution into account, and does not require physical model tests to obtain τ_c and ω. A new method of suffusion simulation is introduced here, whereby the particles are considered separately with a multiphase flow simulation according to their different sizes. Concurrently, the particle transport is considered by using an advection equation in which the particle flow velocity is calculated by a momentum balance equation. In this paper, the fundamental assumption of suffusion is the particle transport, which is mainly induced by drag force, governed by the advection equation. Hence, the particle transport can be more realistically expressed than by just replacing the particle flow velocity with the fluid flow velocity.

As for the notations and symbols in this paper, the bold letters denote vectors, "$\cdot$" denotes the inner product of two vectors (e.g., $\mathbf{a} \cdot \mathbf{b} = a_i b_i$), "$|\ \ |$" denotes the norm of a first-order tensor (e.g., $|\mathbf{a}| = \sqrt{\mathbf{a} \colon \mathbf{a}} = \sqrt{a_i a_i}$), "$\dot{\ }$" denotes the time derivative, and subscript zero denotes the initial state (e.g., v_0 = initial specific volume).

Methodology

Simulation concept
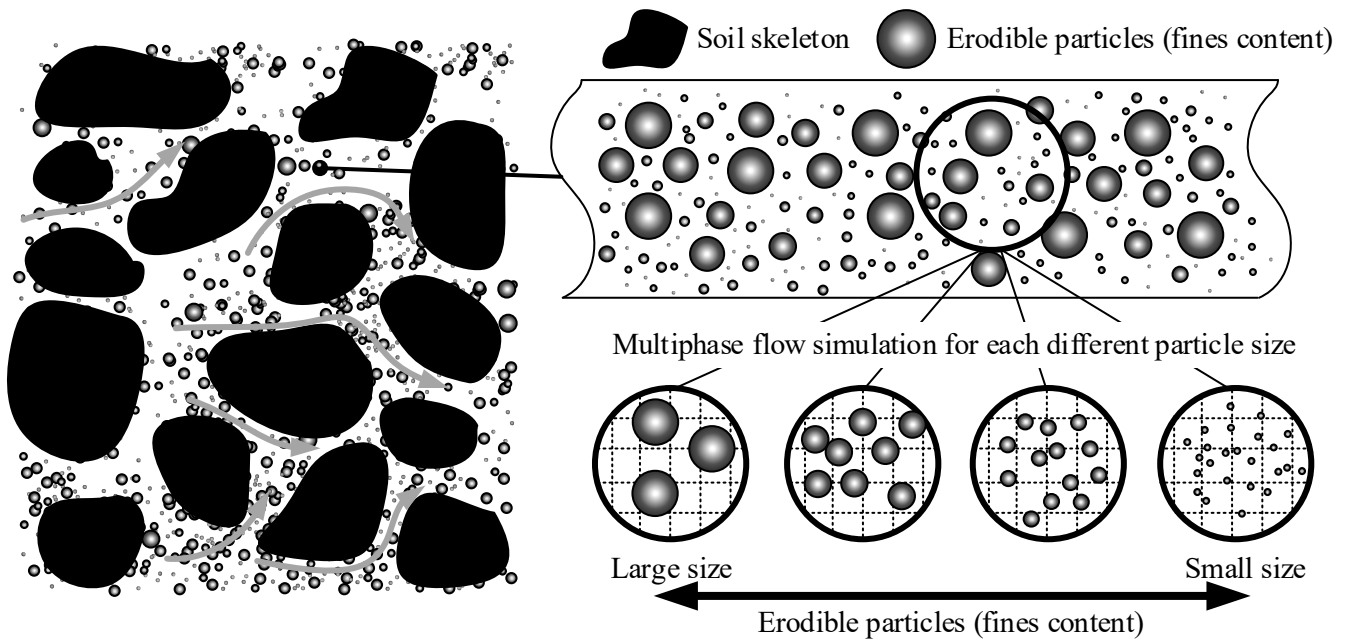
Fig. 1. Concept of multiphase flow simulation for different grain sizes

Fig. 1 describes the proposed concept of the multiphase flow simulation with ideally gap-graded soil. The purpose of the newly proposed concept is to explain the particle transportation in suffusion by taking into account the particle flow in correspondence to the grain size distribution. Thenceforth, this numerical simulation requires the physical properties and particle size distribution of the soil.

Advection is the movement of bulk motion which might drag or carry some substances, such as particles, along with the majority of the advected substances. Therefore, the particle transport through porous media by the water flow motion, considered to comprise the majority of the advected substances, is described by the advection equation [23, 24, 25, 26]. Advection is basically derived from the conservation law in the scalar field. In addition, the advection in the present simulation was used to describe the particle substance flow. Moreover, the mass of each particle size index, divided according to size, is accordingly conserved. Therefore, the total erodible particle flow or inactive fines are explicitly conserved as well. According to the partial differential equation of advection, **Eq. (2)**, the velocity of the particles, $\mathbf{u_e^i}$, represents the particle flow velocity or the erodible particle velocity of the erosion phenomena.

$$\dot{\varphi}_i + \mathbf{u_e^i} \cdot \boldsymbol{\nabla}\varphi_i = S_\varphi \qquad (2)$$

where φ_i is the concentration of erodible particles or inactive fine particles, and S_φ is the source term which represents the exchange rate between the non-erodible and the erodible fractions. Subscript n means the difference in particle size. The inactive fine particles, the mobile particles, are considered to be erodible particles and detachable from the soil mass. Furthermore, the ratio between the active and the inactive fine particles is strongly dependent on the confining stress and the seepage flow, but which is also out of the scope of this research [27, 28]. Therefore, the concentration of inactive fine particles is described by the following experimental conditions. The velocity term — an essential part of the advection equation — controls the speed of the substance transportation, resulting from the drag force calculation.

Drag force is the force that comes from the difference between the pressure in the front region and that in the back region [29]. Basically, the particles flowing in the fluid phase, namely, the flow surrounding the particles, exert a different drag force on the particles and greatly depend on the particle size, sphericity, and current flow velocity of the particles [30]. Therefore, a multiphase flow calculation is preferable to suffusion modeling (based on the continuum method) because it considers the particle size distribution and the different particle flow velocities of the different particle sizes.

According to the particle transport, particles of different sizes would travel at different speeds under the same motion of fluid flow, namely, the majority of the advected substances. The erodible particle flow is described separately under the advection equation and corresponds to subscript n in the equation. The soil model is considered as a three-phase model: 1. Fluid, 2. Erodible soil, and 3. Soil skeleton. The erodible particles are divided into several fractions according to the different sizes of particles, as shown in **Fig. 2**.
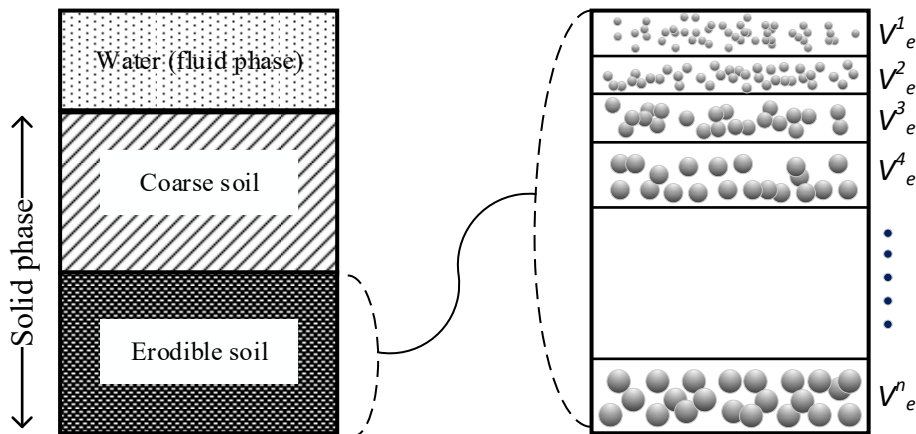
Fig. 2. Concept of soil model for erosion calculation

Therefore, the total volume of the soil mass, V_T, should be the summation of the erodible soil, soil skeleton, and fluid volume, as given by **Eq. (3)**.

$$V_T = V_e + V_s + V_{void} \qquad (3)$$

where V_e is the volume of the erodible soil, V_s is the volume of the soil skeleton, and V_{void} is the volume of the fluid.

Furthermore, the volume of erodible particles must be divided into several groups to represent the individual sizes of the erodible particles in a narrow range. Hence, V_e must be replaced by the following relationship:

$$V_e = \sum_{i=1}^{n} V_e^i \qquad (4)$$

where V_e^i is the volume of erodible particles in group i. In addition, the particles are divided into n groups in accordance with the sieve analysis obtained from experiments. Letting the mesh in the sieve analysis be n in size, with D_i representing the opening size of the mesh which is in the range $[1, n]$, while D_0 stands for size 0 in diameter, the total volume of particles in group i or V_e^i is the summation of the volume of the particle size in the range $(D_{i-1}, D_i]$.

According to previous research on the particle flow, the utilization of the drag force from the aerodynamic law always shows promising results in many research fields [31, 32, 33]. In this research, the drag force is mainly associated with the force calculation which stimulates the particles to flow. In addition, the drag force is proportional to the square of the relative velocity between the fluid, $\mathbf{u_f}$, and the particles, $\mathbf{u_p}$, as shown by **Eq. (5)** [29, 34].

$$\mathbf{F_D} = \frac{1}{2}\rho_f C_d A_p \left| \mathbf{u_f} - \mathbf{u_p} \right| (\mathbf{u_f} - \mathbf{u_p}) \qquad (5)$$

where, A_p is the cross-sectional area of the particles and C_d is the drag force coefficient.
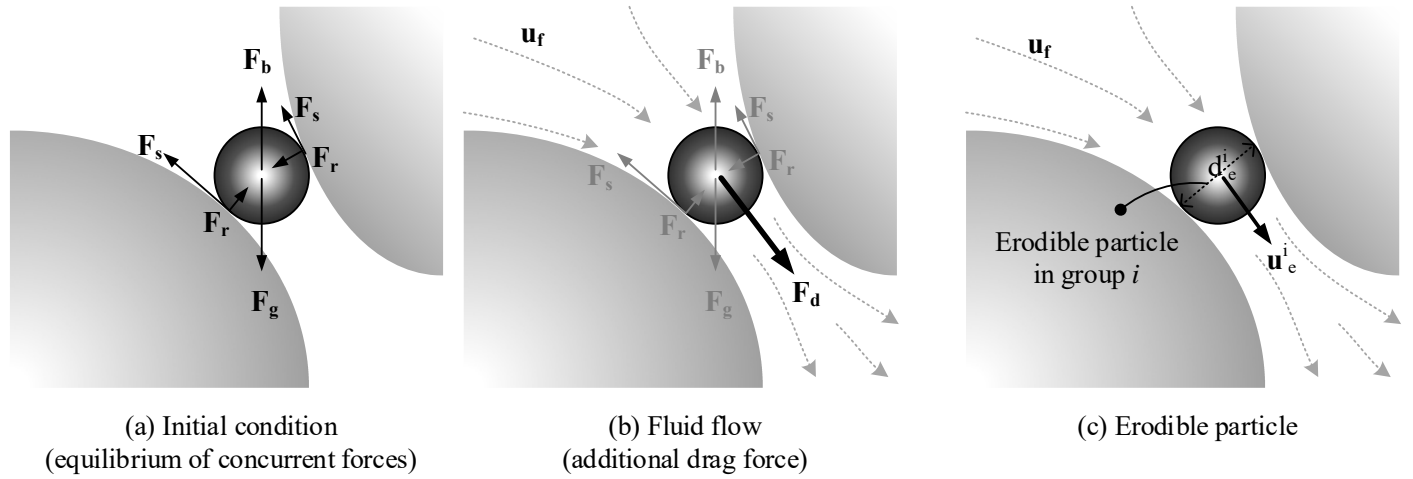
Calculation Scheme
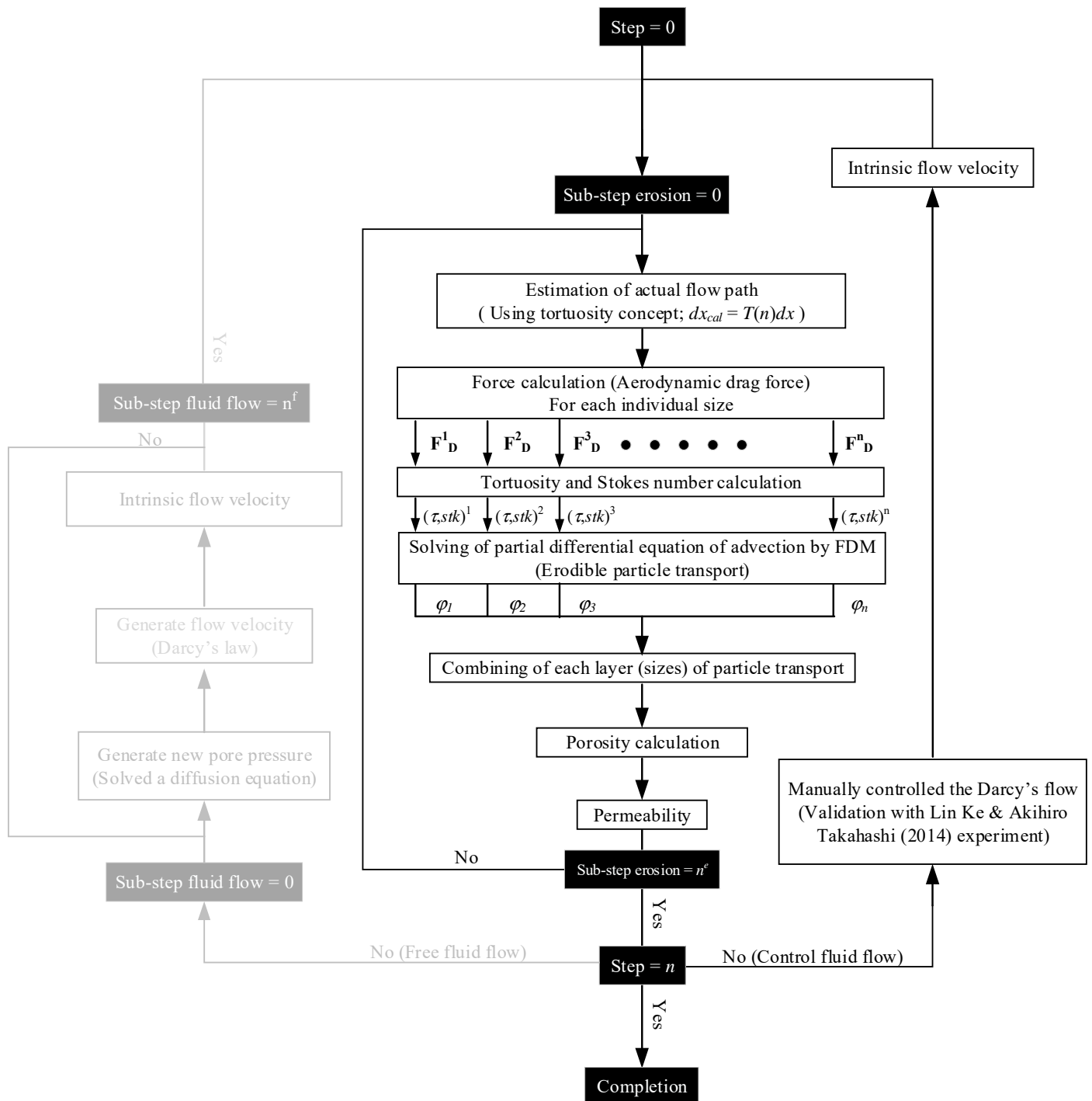
Fig. 3. Flowchart of erosion calculation

Fig. 3 shows the erosion calculation scheme, including two main paths which are different in the fluid flow calculation; the fluid flow velocity can be either numerically or manually determined. According to the experiment by Ke & Takahashi (2014), the fluid flow through porous media is technically controlled [35]. Therefore, the fluid flow was manually determined here, corresponding to the experiment.

The forces acting on the erodible particles inside the porous media at the initial stage (without seepage flow) might be the gravitational force (F_g), buoyant force (F_b), frictional force (F_s), and reaction force (F_r) from the soil skeleton. It could also be implied that, at the initial stage without moving particles, the summation of these forces results in an equilibrium, as seen in **Fig. 4(a)**. While the fluid starts to flow, drag force is generated on each erodible particle, which causes the particle movement seen in **Fig. 4(b)**. Therefore, the purpose of this numerical calculation of suffusion is to emphasize the additional force—drag force—exerted by the fluid flow on the mobile particles. There are several factors effecting the drag force; the size of the particles is one of them and it is the main influence on the drag force. Hence, the drag force $\mathbf{F_D^i}$ on each particle size is individually calculated. In addition, the original drag force equation, **Eq. (5)**, was originally developed to consider a single particle flow, which means it is not capable of considering a group of particle flows. Consequently, **Eq. (5)** alone cannot be used to estimate the drag force of the particle flows in porous media related to this research in which the particle phase fraction must be taken into account.

(a) Initial condition
(equilibrium of concurrent forces)

(b) Fluid flow
(additional drag force)

(c) Erodible particle

**Fig. 4.** Concurrent force acting on erodible particle in porous media

Fortunately, the relationship between the particle volume fraction and the drag force coefficient has been illustrated [36]. In addition, Rusche and Issa (2000) recommended that the effect of the particle volume fraction on the drag force be included in the calculation of the drag force [37]. Hence, the multiplier of the drag force coefficient, $f(\alpha)$, was added to the equation, as shown in **Eq. (6)**, as a consequence of the effect of the phase fraction.

$$\mathbf{F_D^i} = \frac{1}{2}\left[f(\alpha)C_D^i\right]\left[\frac{\pi}{4}\left(d_e^i\right)^2\right]\rho_f\left(\mathbf{u_e^i} - \mathbf{u_f}\right)\left|\mathbf{u_e^i} - \mathbf{u_f}\right| \qquad (6)$$

where C_D^i is the drag force coefficient for a single particle flow, $f(\alpha)$ is the multiplier of the drag force coefficient, d_e^i is the diameter of an erodible particle, ρ_f is the density of the fluid, $\mathbf{u_e^i}$ is the particle velocity, $\mathbf{u_f}$ is the fluid velocity, and subscript i represents each particle group (size). In addition, the multiplier of the drag force coefficient, $f(\alpha)$, is a function of particle fraction α, which has the following relationship, **Eq. (7)**:

$$f(\alpha) = \exp(K_1\alpha) + \alpha^{K_2} \qquad (7)$$

where α is the particle phase fraction, and K_1 and K_2 are the coefficients for which 2.68 and 0.43, respectively, are recommended in accordance with the particle flow in the solid-liquid system [37]. Fig. 5 shows that the increment in the particle phase fraction has a positive effect on the value of the drag force multiplier. In addition, the lower boundary of the particle fraction is zero and the drag force multiplier becomes 1.0 which is concurrent with the original drag force for a single particle flow.
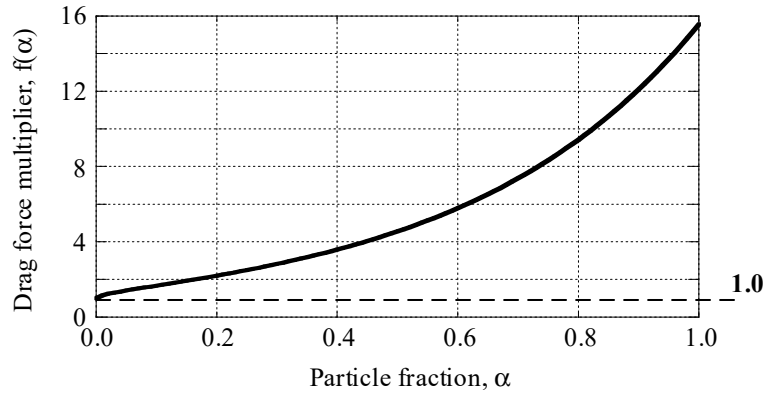
Fig. 5. Relation between particle fraction and drag force multiplier

The drag force coefficient refers to the number that mainly considers the complex effect of the physical properties of the particles on the drag force. Several suggestions have been made for the drag force coefficient, especially for the case of a single particle flow in the fluid phase. The drag force coefficient depends on the particle size, particle shape, viscosity of the fluid, and fluid density. It is sometimes known as a function of the Reynolds number, *Re*, which is calculated by **Eq. (8)** [31]. The linear estimation of the drag force coefficient by the Reynolds number, $\frac{24}{Re}$, is capable under a low seepage flow. However, when the Reynolds number becomes greater than 0.3, the relation is not nonlinear [38]. Furthermore, the drag coefficient decreases with the inclination of the Reynolds number, as shown in **Fig. 6**. Several researchers have proposed either continuous or discontinuous functions for the drag force coefficient [38, 39]. In this paper, the continuous function, covering a wide range of Reynolds numbers, suggested by Haider & Levenspiel (1989), is applied under the assumption of spherical particles [40, 41], as seen in **Eq. (9)**.
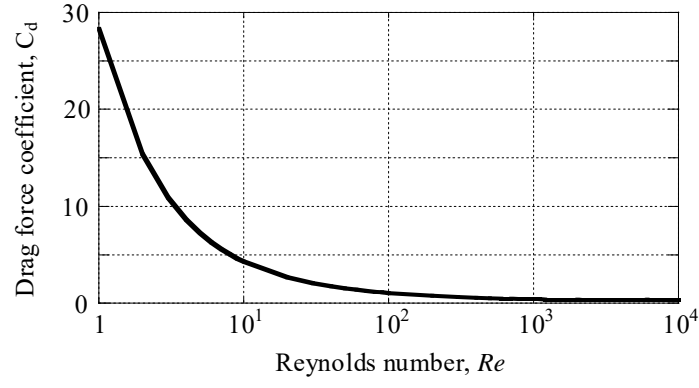
Fig. 6. Relationship between Reynolds number and drag force coefficient (Haider & Levenspiel, 1989)

$$Re = \frac{\rho_f |\mathbf{u_f} - \mathbf{u_e^i}| d_e^i}{\mu_f} \tag{8}$$

where ρ_f is the fluid density, $|\mathbf{u_f} - \mathbf{u_p}|$ is the size of the relative velocity between the fluid and the particles, d_e^i is the particle diameter, and μ_f is the dynamic viscosity of the fluid. Then, the Re of each erodible particle is defined. Therefore, in the present analysis, C_D^i is re-defined as $C_{D,sphere}^i$ under the spherical assumption of each soil particle. The drag force coefficient of the spherical particles is empirically obtained as follows:

$$C_D^i = C_{D,sphere}^i = \frac{24}{Re}(1 + 0.1806 Re^{0.6459}) + \frac{0.4251}{1 + \dfrac{6880.95}{Re}} \tag{9}$$

The particle velocity, required in the advection equation, can be obtained from the force and the velocity equation or the conservation of momentum, as given in **Eq. (10)**. The force calculation, which is calculated from only the drag force, will be substituted into the momentum conservation equation. In addition, the mass can be calculated by using the relation among the mass, density, and volume, as shown in **Eq. (11)**. Subsequently, the new velocity of the particle flow can be updated in accordance with **Eq. (12)**.

$$\mathbf{F_D^i} = m^i \dot{\mathbf{u}}_e^i \tag{10}$$

$$m^i = \rho^i V_{vol}^i = \rho^i \frac{4}{3}\pi (d_e^i)^3 \tag{11}$$

$$\dot{\mathbf{u}}_e^i = \frac{(\mathbf{u_e^i})^t - (\mathbf{u_e^i})^{t-\Delta t}}{\Delta t} \tag{12}$$

In this research, the partial differential equation, shown as Eq. (2), stands for the particle transportation and will be numerically calculated. According to the advection form of the particle flow, the finite difference method (FDM) is applied to solve the partial differential equation which is desirable enough for mass conservation. Unfortunately, one of

the main drawbacks of the FDM is the calculation of irregular elements. However, the simulation in this research has been conducted with elements of a uniform size. Hence, the concentration of each particle size is obtained by solving the partial differential equation for advection by the finite difference method.

According to the fluid flow velocity, which was used to formulate the drag force and is referred to as the intrinsic flow velocity in this study, consideration must be given to the changes in porosity since porosity greatly influences the intrinsic flow velocity. Erosion means the amount of erodible particles that disappear. Hence, both the erodible particle volume change, ΔV_e, and the volumetric strain, ε_v, affect the porosity change, $\Delta \emptyset$, as shown in **Eq. (13)**. Subsequently, the porosity is updated by **Eq. (14)**.

$$\Delta V_e = V_T \varepsilon_v - \Delta \emptyset \tag{13}$$

$$\emptyset^t = \emptyset^{t-\Delta t} + \Delta \emptyset - V_T \varepsilon_v \tag{14}$$

Furthermore, the loss of erodible particles in each soil element can be calculated from the difference between the residual erodible particles and the volume of erodible particles at the previous step, as given in **Eq. (15)**.

$$\frac{\Delta V_e}{V_T} = \sum_{i=1}^{n} \varphi_i^t - \sum_{i=1}^{n} \varphi_i^{t-\Delta t} \tag{15}$$

where φ is the concentration of erodible particles obtained by solving the advection equation by the finite difference method, subscript n means the particle group, following the diameter or size, and t shows the current time step or previous step of the calculation, $t - \Delta t$.

Moreover, the thought of the intrinsic flow velocity was addressed; it explicitly affects the drag force on the erodible particle flow. Therefore, the average flow or Darcy flow velocity obtained from the numerical calculation or experimental condition (validation with Lin Ke & Akihiro Takahashi, 2014) must be adjusted, as seen in **Eq. (16)** [42].

$$\mathbf{u_f} = \frac{\mathbf{u_0}}{\emptyset} \tag{16}$$

where $\mathbf{u_0}$ is the average flow velocity or Darcy flow velocity, and $\mathbf{u_f}$ is the intrinsic flow velocity which will be used in the drag force calculation.

According to the consideration given to the particle flow in porous media, the soil skeleton or coarse particles are obstructive and prevent the erodible particles from flowing perfectly along the fluid flow direction in the macroscopic scale. Hence, the total distance of the particle flow is not the same as the length of the system in the flow direction. In order to predict the distance of the actual flow path, the concept of tortuosity is used [43]. There are several suggestions on tortuosity for porous media in which the tortuosity, T, is generally a function of porosity, $\emptyset$ [44]. Mostly, different

functions of tortuosity represent different types of media, such as $T(\emptyset) = \emptyset^{-p}$ and $T(\emptyset) = 1 - p \ln \emptyset$ used for the electric field and spherical particles, respectively, where the p-value depends on the material properties [45, 46]. The relation that is often used for soil materials is governed by either $T(\emptyset) = [1 + p(1 - \emptyset)]^2$, which is specifically used for mud, or **Eq. (17)** [47]. Furthermore, the previous research confirmed that the general form for the tortuosity function used for soil materials is shown in **Eq. (17)** in which the p −value is within the range of 2.0 to 3.0 [48]. Therefore, in the simulation done in this paper, the tortuosity in **Eq. (17)** is used to represent the tortuosity in porous media.

$$T(\emptyset) = 1 + p(1 - \emptyset) \tag{17}$$

According to the concept of tortuosity, the ratio between the actual flow path, L_p, and the system length, L_0, can be concluded as a function of porosity. In addition, the inclination in porosity causes increases in the tortuosity or extension of the actual flow path, as seen in **Fig. 7**. The element length in the discretization for an advection equation is adjusted to correspond with the estimated flow path at every calculation step. Therefore, the tortuosity multiplier is used to extend the size of the element, in order to consider the actual length of the transported particle in each element, by following **Eqs. (18) and (19)**.
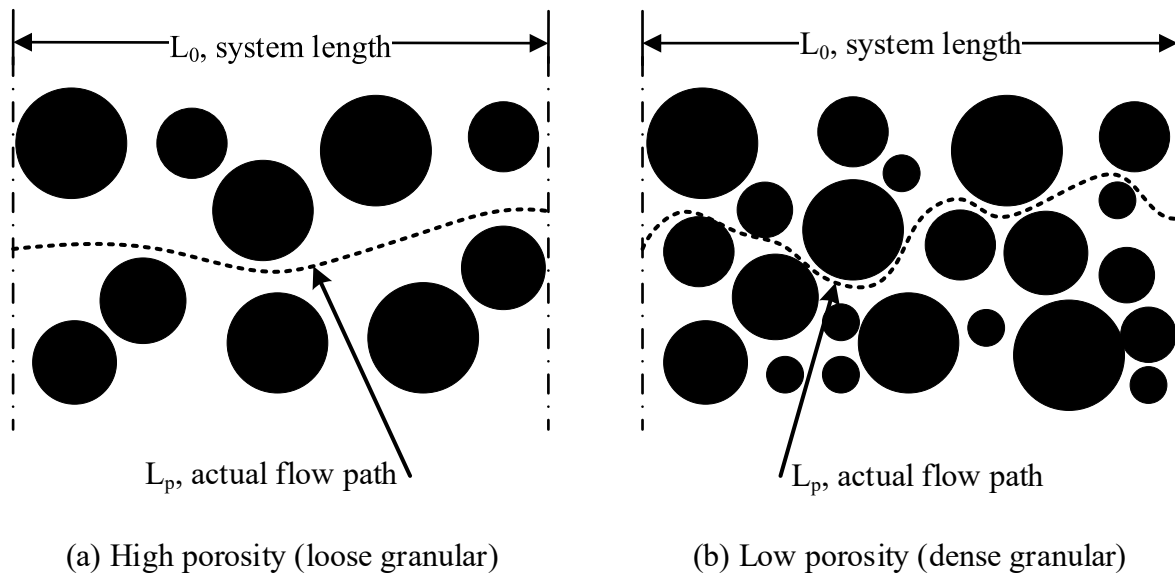
Fig. 7. Concept of tortuosity for actual flow path of particles

$$dl = T(\emptyset)dl_0 \tag{18}$$

where dl_0 is the size of the original element in accordance with the domain or the size of the soil mass in which dl is either dx or dy.

In order to capture the time-dependent particle flow in porous media, it might be necessary to consider the Stokes number and the clogging process in accordance with the difference in time scales between the fluid flow phase and the particle

flow phase. In general, the Stokes number is a dimensionless parameter and represents the relaxation time or the stopping time between those two phases. A simplification of the form is shown in **Eq. (19)** [49].

$$stk = \tau = \frac{t_p}{t_{flow}} \tag{19}$$

where t_p is the particle stopping time and t_{flow} is the characteristic time of the fluid flow.

Several suggestions have been made for calculating the Stokes number depending on the application [49, 50, 51, 52]. The Stokes number for solid particles suspended in fluid, or the solid-fluid phase, can sometimes be a function of the Reynolds number, as shown in **Eq. (20)** [53].

$$\tau = \eta Re = \frac{\rho_s}{\rho_f} Re = \frac{\rho_s}{\rho_f} \frac{\rho_f |\mathbf{u_e^{avg}}| d_e^i}{\mu_f} \tag{20}$$

where η is the solid-to-fluid density ratio, ρ_s is the density of a particle, ρ_f is the fluid density, $\mathbf{u_e^{avg}}$ is the average fluid flow velocity, d is the particle diameter, and μ_f is the dynamic viscosity of the fluid.
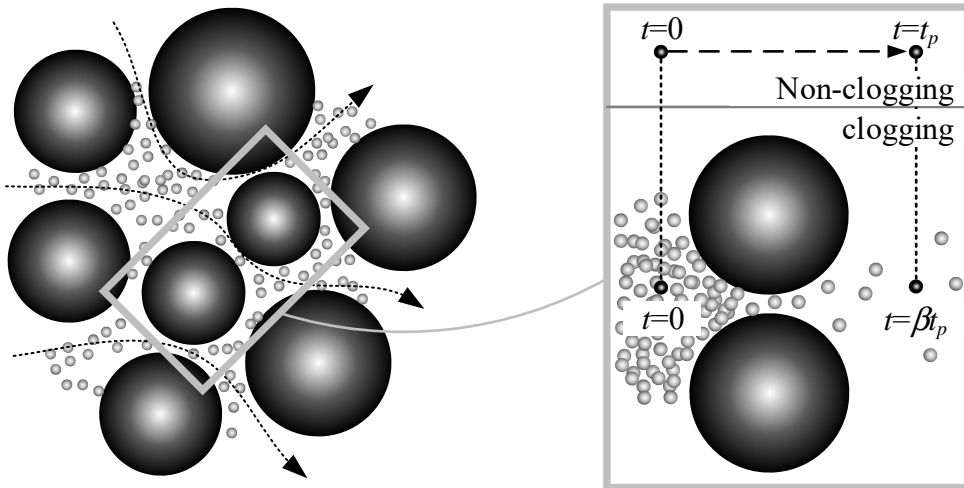
Fig. 8. Clogging process in porous media

Although particle clogging in porous media is unavoidable, due to constriction, previous research has shown that fortunately the clogging process will increase the arrest time lapses which are basically normalized by the Stokes number [54, 55]. In general, clogging can often be found where the particles move through a bottleneck, as shown in **Fig. 8**, and the particle congestion forms at the entrance channel. Nevertheless, the arrest time lapses normalized by the Stokes number, $\frac{T_a}{\tau}$, still cannot be expressed in a function for the constriction size. Hence, in order to include the clogging process inside porous media, constant parameter β_{clog}, considering the clogging relaxation time, will be used to calculate the arrest time lapse, T_a, as seen in **Eq. (21)**.

$$T_a = \beta_{clog}\tau \qquad\qquad (21)$$

Therefore, the advection discretization for each particle size domain under the finite difference method can be performed by the different time scale, $t_i^* = \frac{t}{T_{a_i}}$, in accordance with the different arrest time lapses of each particle i index, T_{a_i}, as shown in **Eq. (22)**.

$$\frac{\partial \varphi_i}{\partial t_i^*} + \mathbf{u_i} \cdot \boldsymbol{\nabla}\varphi_i = S_\varphi \qquad\qquad (22)$$

Numerical calculation

Parameter and numerical model simulation referring to Ke and Takahashi (2014) experiment
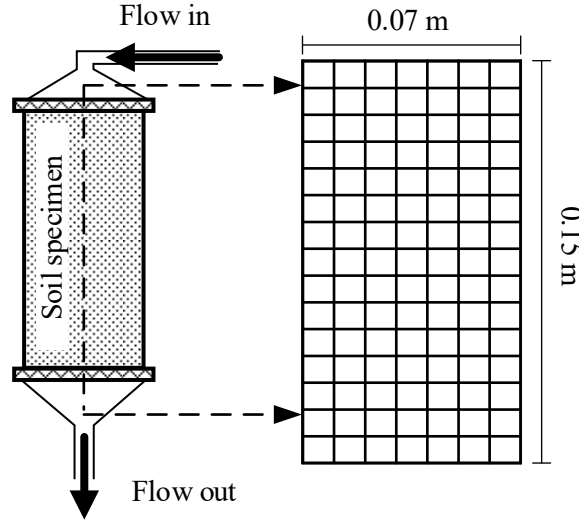
Fig. 9. Size of specimen from Ke and Takahashi (2014)

The proposed numerical framework requires a strict validation of this numerical model when conducting the suffusion simulation. Therefore, the aim of this simulation is to confirm the validity of the numerical method by comparing it against the experimental data from the research work by Ke and Takahashi (2014). The numerical calculation was conducted with the size of the domain in accordance with the experimental conditions seen in **Fig. 9**, namely, 0.07 m in width and 0.15 m in length. In addition, the data from a sieve analysis on the two different types of silica sand were necessary to consider the multiphase flow.

Table 1. Parameters

Physical property	
Specific gravity of soil, G_s	2.645
Fines content of each particle index, φ_i^t	Distribution curve of grain size (Fig. 11)
Initial void ratio, e_0	As shown in Table 2
Inactive fines content ratio, φ_i/φ_i^t	As shown in Table 2
Fluid density (water), ρ_f	$1000\ kg/m^3$
Dynamic viscosity, μ	$0.8 \times 10^{-3}\ Pa \cdot s$
Parametric study	
Constant value in tortuosity function, p	
Clogging relaxation time, β_{clog}	

Table 1 summarizes the necessary parameters for the proposed numerical simulation. As seen in the table, this research pays more attention to the particle size distribution. **Fig. 10** shows the grain size distribution of silica sand Nos. 3 and 8 in both accumulative and distribution curves. Silica sand No. 8, or fine sand, falls in the range of sizes smaller than 1 mm and is considered to comprise erodible particles. The initial void ratio obtained from the experiment is transformed to a porosity value for the numerical calculation by its relationship, $\emptyset = \frac{e}{1+e}$. As mentioned earlier, this research does not consider the stress effect; therefore, the inactive fines content ratio, φ_i/φ_i^t, will be manually assigned to the simulation as well. Consequently, the soil skeleton, or immobile particles, remains inside the soil mass and is composed of coarse materials. The particles are larger than 1 mm in size and there is an active fines content. On the other hand, in Ke and Takahashi's experiment, three mixtures of silica sand were utilized for suffusion testing, following the proportions listed in **Table 2**. **Fig. 11** show the particle size distribution which is subsequently obtained from the accumulative curve. Hence, the inactive fines content or mobile particles can be calculated and assigned to the simulation.

(a) Accumulative curve   (b) Distribution curve
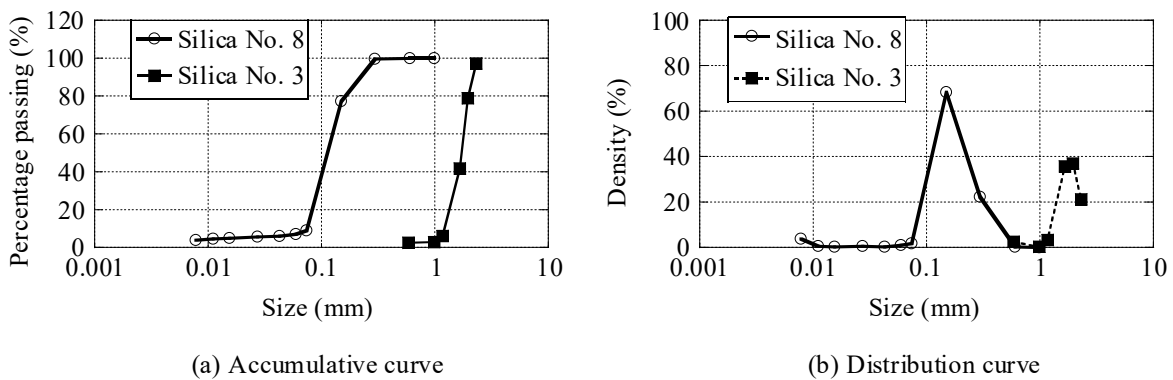
Fig. 10. Grain size distribution curves of silica sand Nos. 3 and 8 from Ke and Takahashi (2014)

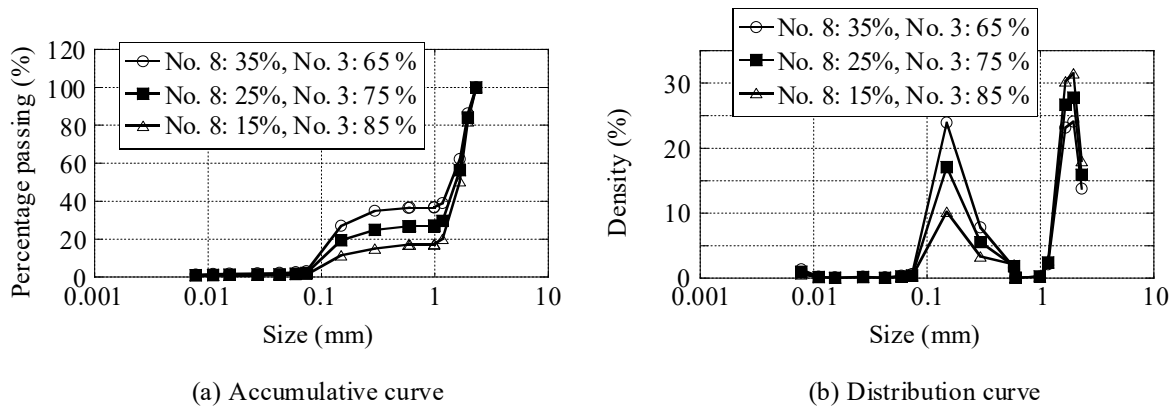(a) Accumulative curve (b) Distribution curve

Fig. 11. Grain size distribution curves of soil mixtures from Ke and Takahashi (2014)

Table 2. Contents of soil mixtures

	1st mixture	2nd mixture	3rd mixture
Fine grain (No. 3)	0.35	0.25	0.15
Coarse grain (No. 8)	0.65	0.75	0.85
Initial void ratio, e_0	0.64	0.61	0.68
Inactive fines content ratio	0.73	0.63	0.52

The proposed erosion calculation must define the range in erodible particle sizes. The solid phase can be separated into two groups: 1. Erodible particles and 2. Soil skeleton. In the Ke and Takahashi (2014) experiment, the opening size of the filter was determined as the maximum size for fine grain, namely, about 1 mm. Therefore, the size of the erodible or fines fraction must be less than 1 mm in accordance with the experimental conditions.
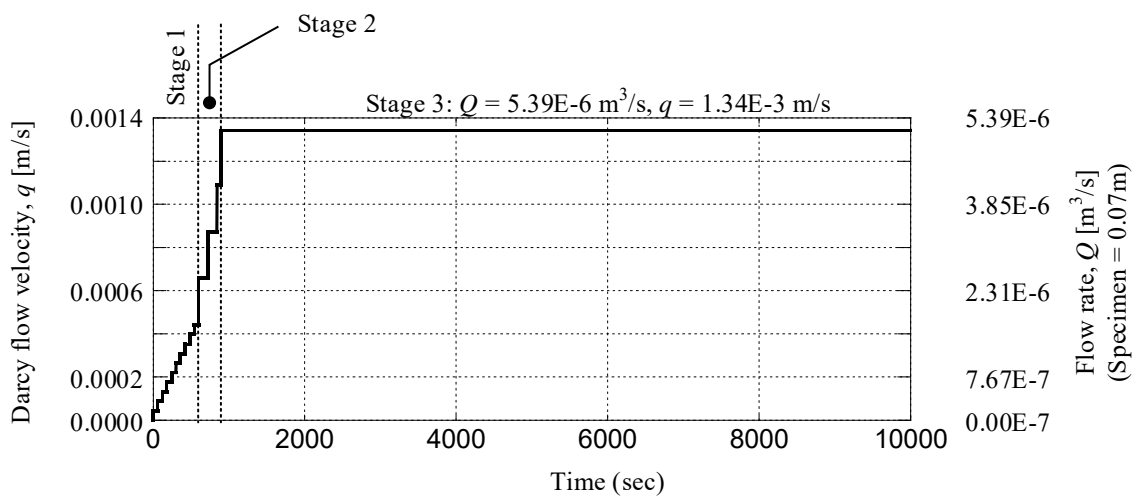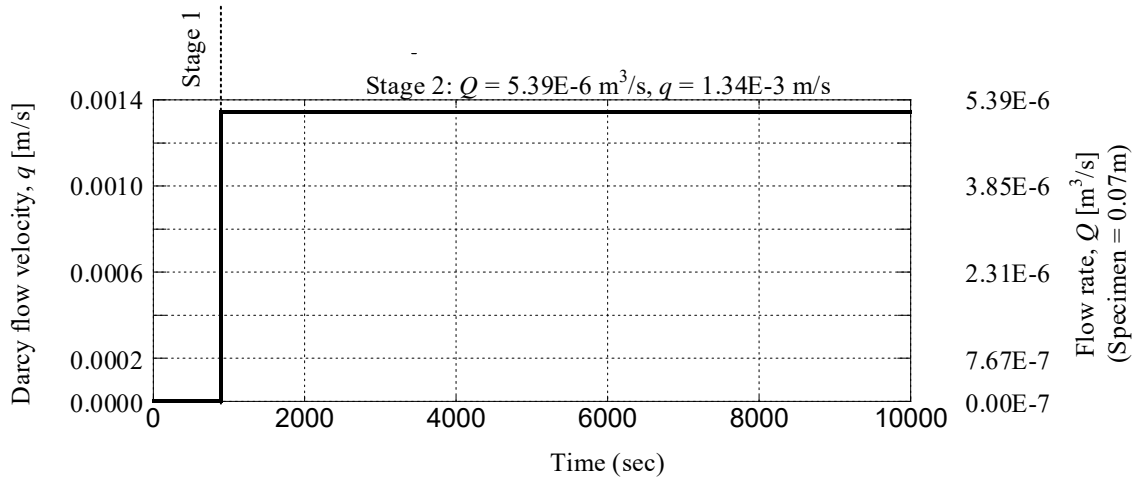

**Fig. 12**. Flow rate in tests by Ke and Takahashi (2014)

**Fig. 13**. Fluid flow for considering initial erosion

The experiment was performed under a steady flow condition and, depending on the purpose, the fluid flow was conducted in three main stages, as shown in **Fig. 12**. Ke and Takahashi (2014) targeted the maximum flow rate at about 5.17E-6 [m³/s] with a specimen 0.07 m in diameter at the final stage (Stage 3). The results from Ke and Takahashi (2014) show that the initiation of erosion is likely to occur at the beginning of Stage 3. Therefore, the modified fluid flow curve will be applied in the simulation as well in accordance with the initiation of erosion in the experiment, as seen in **Fig. 13**.

Numerical calculation results and discussion

In this research, two variables, the p-value in the tortuosity function and the clogging relaxation time, β_{clog}, are mainly discussed under two kinds of steady fluid flow, the actual fluid flow and the adjusted fluid flow. According to the concept of tortuosity, the proper function for the sand material is shown as **Eq. (17)** with the p−value in the range of 2 and 3. Hence, the analysis in this paper will be conducted with $T(\emptyset) = 1 + p(1 − \emptyset)$ to make a comparison with the experiment data.
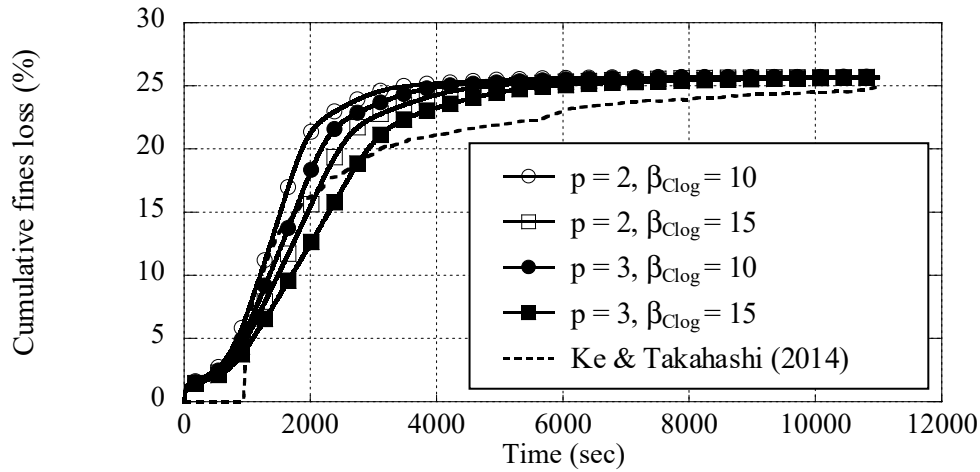
Fig. 14. Calculation with $T(\emptyset) = 1 + p(1 - \emptyset)$ under actual flow condition
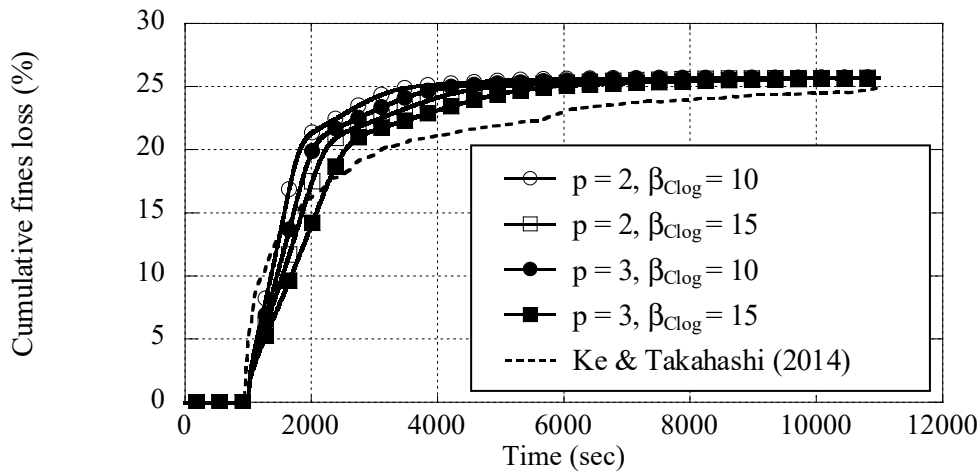
Fig. 15. Calculation with $T(\emptyset) = 1 + p(1 - \emptyset)$ under adjusted flow condition

The first simulation was conducted under the two different flow conditions using a fines content of 35%, as seen in **Figs. 14** and **15**, respectively. The erosion under the actual flow condition, in **Fig. 14**, shows that the cumulative fines loss starts to increase at the beginning of the analysis, while the erosion starts at the same time as the experiment under the adjusted flow condition. The first calculation also shows the different p-values; higher p-values will reduce the erosion rate. In addition, an increase in the clogging time scale, β_{clog}, could cause the erosion rate to slow down. However, some differences still exist between the experiment and the numerical calculation. At the beginning of erosion, the cumulative fines loss from the experiment is higher than that from the calculation. This implies that the erosion rate from the experiment is slightly greater than that from the calculation.
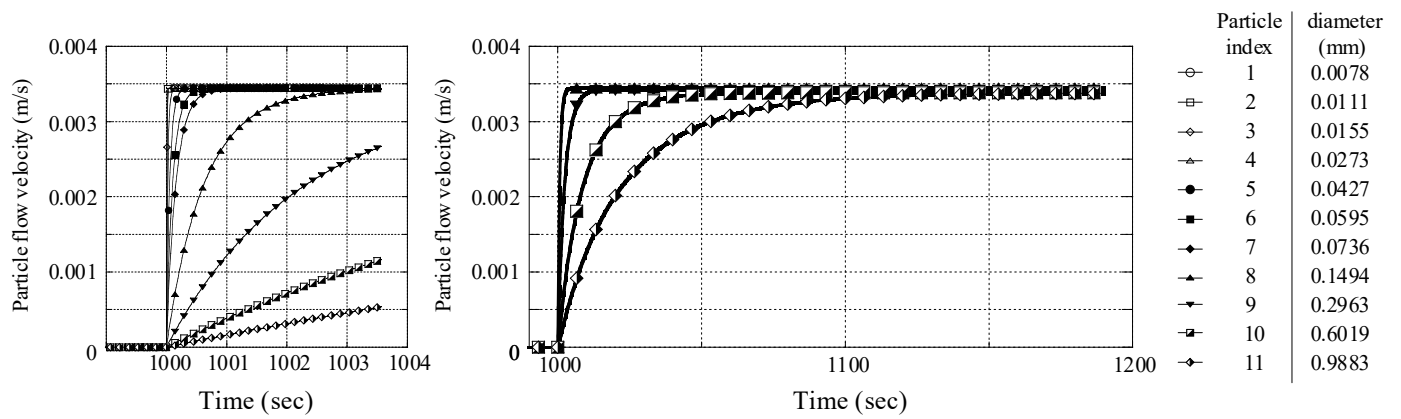
Particle index	diameter (mm)
1	0.0078
2	0.0111
3	0.0155
4	0.0273
5	0.0427
6	0.0595
7	0.0736
8	0.1494
9	0.2963
10	0.6019
11	0.9883

Fig. 16. Particle flow velocity of each particle size in adjusted flow condition ($p = 3$, $\beta_{clog} = 15$)

In addition, the particle flow velocity for each particle size is depicted from the adjusted flow condition in **Fig. 16**. The results show that the velocity of the small particles is likely to increase in a short period of time. Conversely, the velocity of the larger particles seems to be gradually increasing. This evidence also confirms that the force-mass ratio or the acceleration of the smaller particles is greater than that of the larger particles.
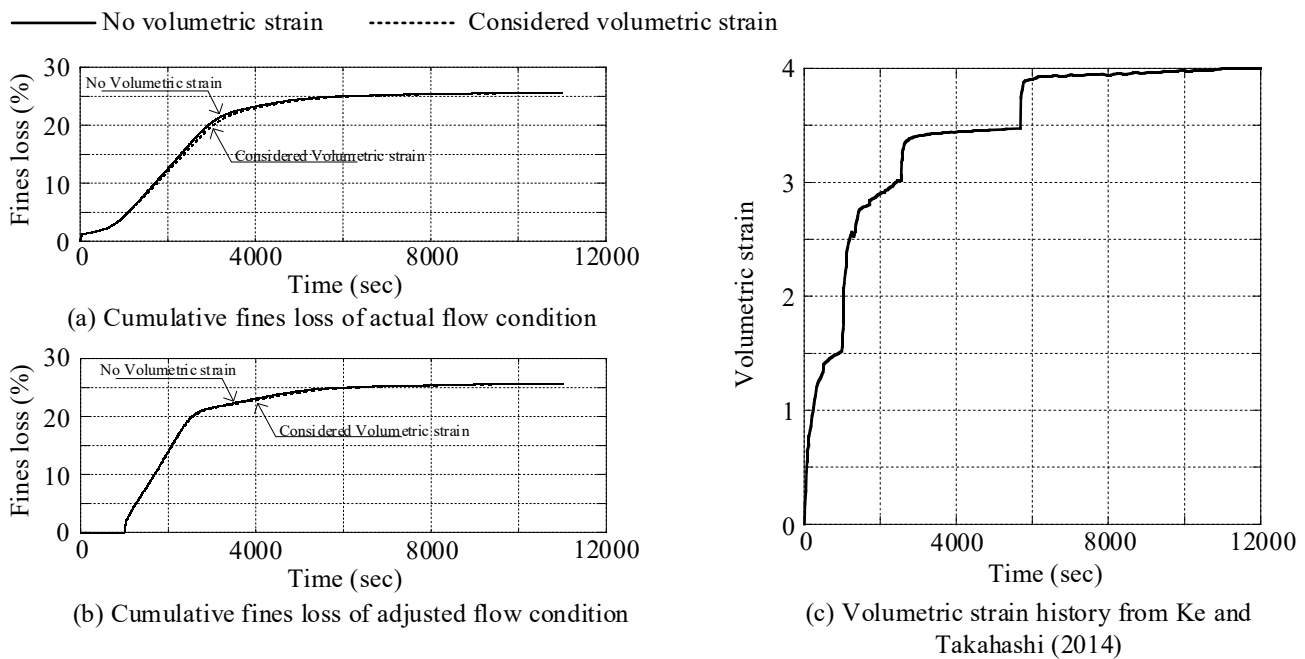

(a) Cumulative fines loss of actual flow condition

(b) Cumulative fines loss of adjusted flow condition

(c) Volumetric strain history from Ke and Takahashi (2014)

Fig. 17. Comparison with and without consideration of volumetric strain ($p = 3$, $\beta_{clog} = 15$)

Volumetric strain is one of the main causes of the changes in the particle flow in both the erosion simulation and the mechanical simulation. Although the current research work does not develop a mechanical calculation scheme for suffusion behavior, changes in the mechanical behavior will have some effect on suffusion through the changes in volumetric strain. Therefore, the effect of volumetric strain will be clarified in this section. Fortunately, the volumetric strain history of the soil sample in Ke and Takahashi (2014)'s experiment shows a fines content of 35%, as illustrated in **Fig. 17(c)**. Therefore, simulations will be conducted by considering the volumetric strain history and disregarding the

volumetric strain in order to elucidate the effect of volumetric strain. Giving consideration to the volumetric strain slightly causes a slowing of the propagation in erosion, which is shown as a cumulative fines loss in **Fig. 17(a) and Fig. 17(b)** for the actual flow and adjust flow conditions, respectively.

According to the experiment, the cumulative fines loss is the primary data, while the erosion rate is considered as the secondary data. The erosion rate is calculated by the ratio between the difference in fines losses and the difference in time increments, $erosion\ rate = \left(\frac{current\ fines\ loss - previous\ fines\ loss}{current\ time - previous\ time}\right)$. In addition, comparisons of the erosion rates between the numerical simulation and the experiment are shown in **Figs. 18** and **19**. The erosion rate from the experiment has a very high value at the beginning of erosion, while the erosion rate from the numerical simulation has a relatively lower value than that of the experiment. In addition, **Fig. 18** shows that the erosion rate under the actual flow condition gradually increases at the beginning of the simulation, due to the gradual increase in the fluid flow velocity, while **Fig. 19** shows that the rate under the adjusted flow condition rapidly increases.

According to the concept of particle transportation, namely, the particles tend to move from the upstream side to the downstream side, the density of the particles should be different at specific locations and times. Furthermore, an examination of the particle size distribution at specific locations and times has been done to show the reduction in each particle size. The simulation results from both the actual and the adjusted flow conditions, for which the clogging time scale was $\beta_{clog} = 15$ and the constant value in the tortuosity function was $p = 2$, were chosen as shown in **Figs. 20** and **24**, respectively. Subsequently, the particle size distributions are presented in **Figs. 21** and **25** and the cumulative curves are presented in **Figs. 22** and **26**. Erosion causes a reduction in the solid fraction in the soil mass which also induces changes in porosity. As mentioned earlier, the consideration of volumetric strain is disregarded in this simulation. Hence, the changes in porosity are directly related to the amount of erodible fines loss. Additionally, the porosity contour at different time steps for both actual flow and adjusted flow cases are separately shown in **Fig. 23** and **Fig. 27**, respectively. According to the particle size distribution and porosity contour results, the reduction in erodible particles starts from the downstream side and the smaller particles tend to become detached from the soil mass sooner, while the larger particles gradually move out of the soil mass.
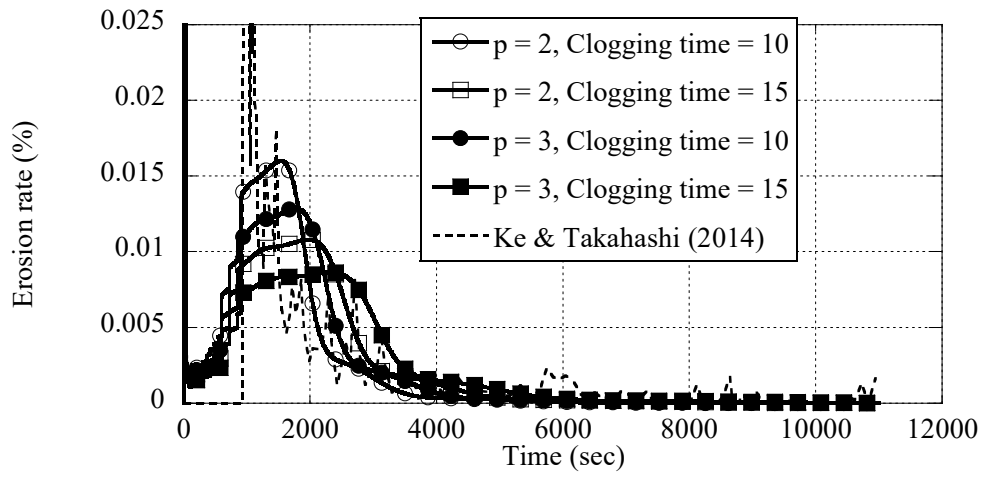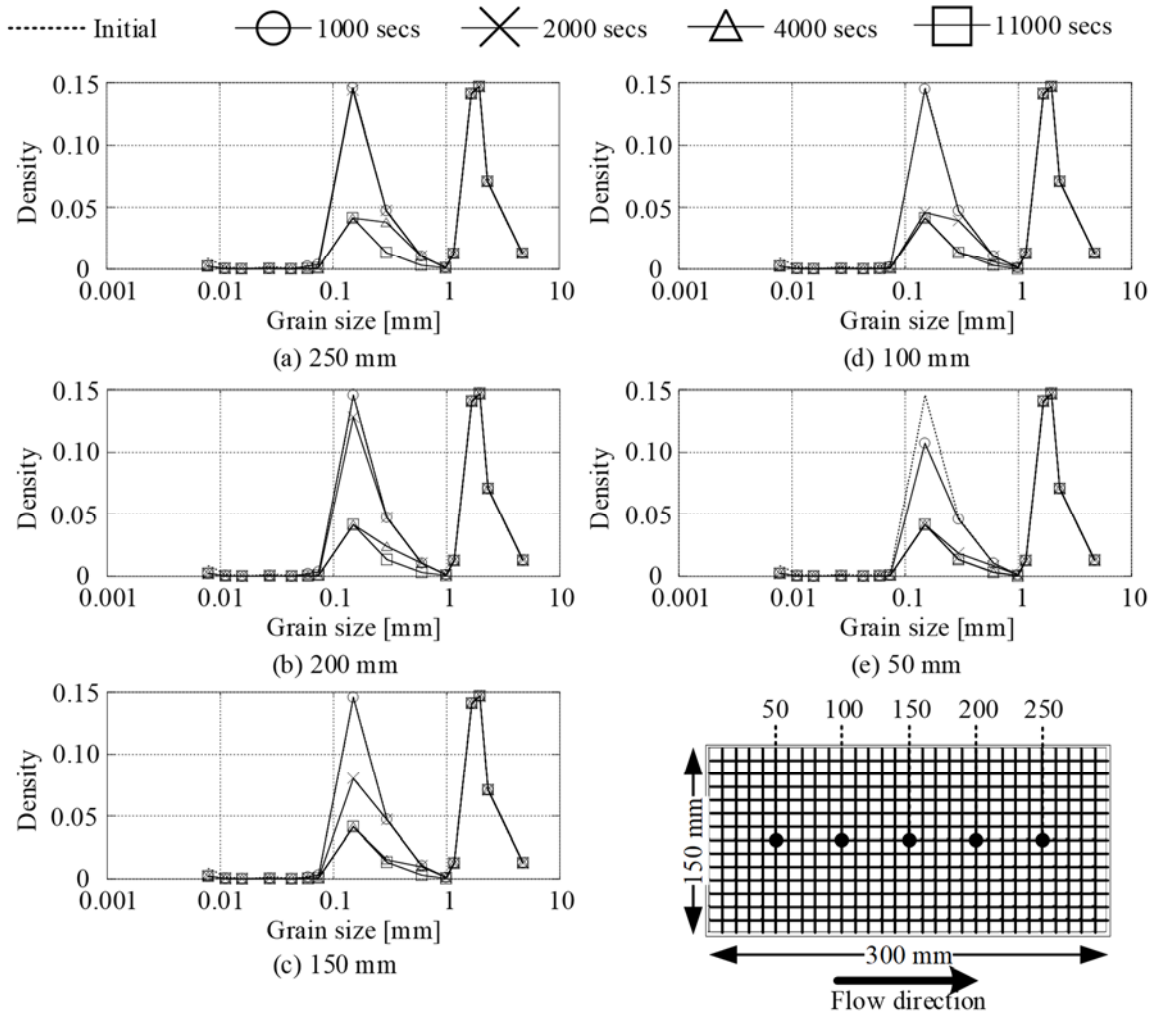
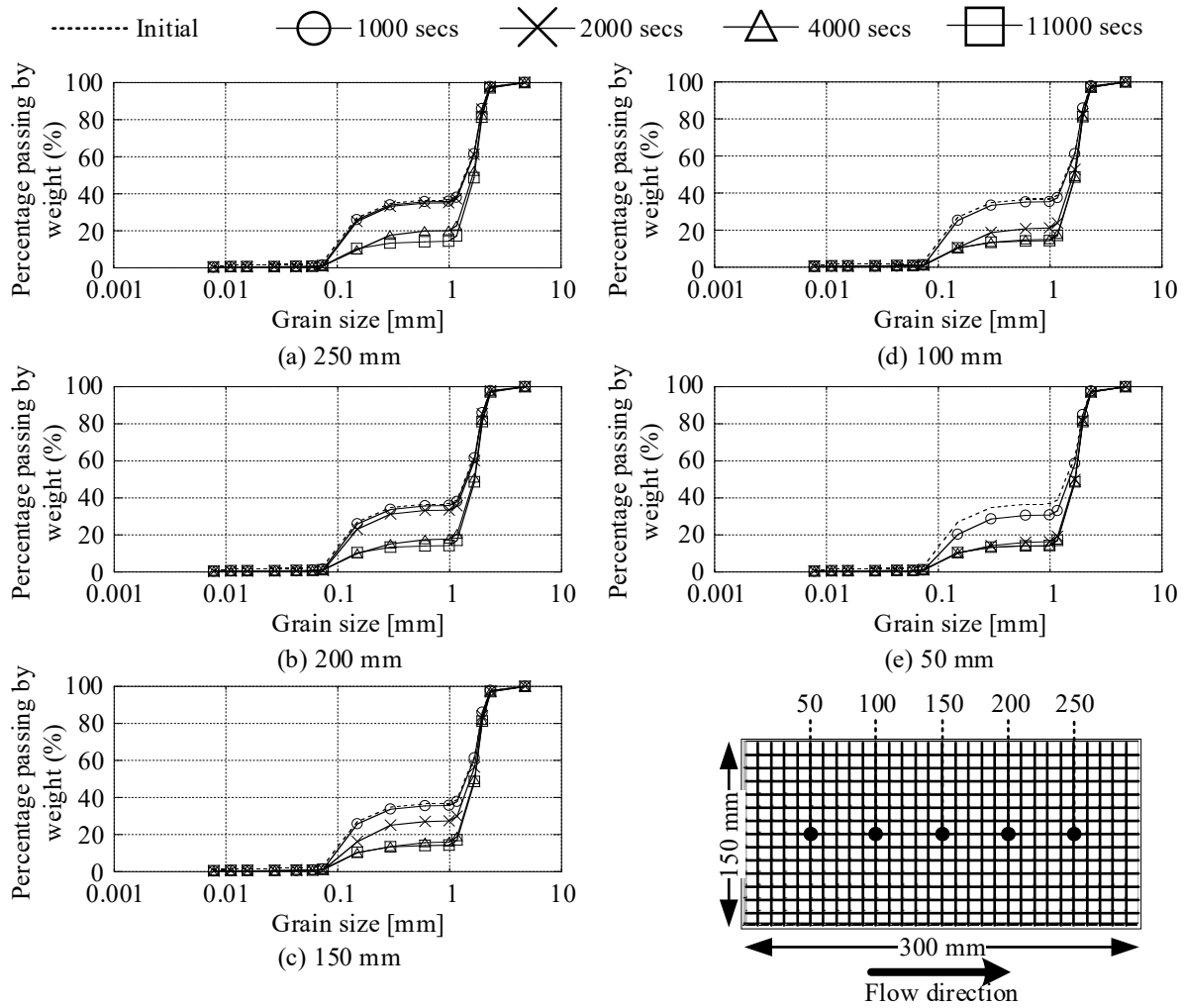**Fig. 18**. Erosion rate under actual flow condition
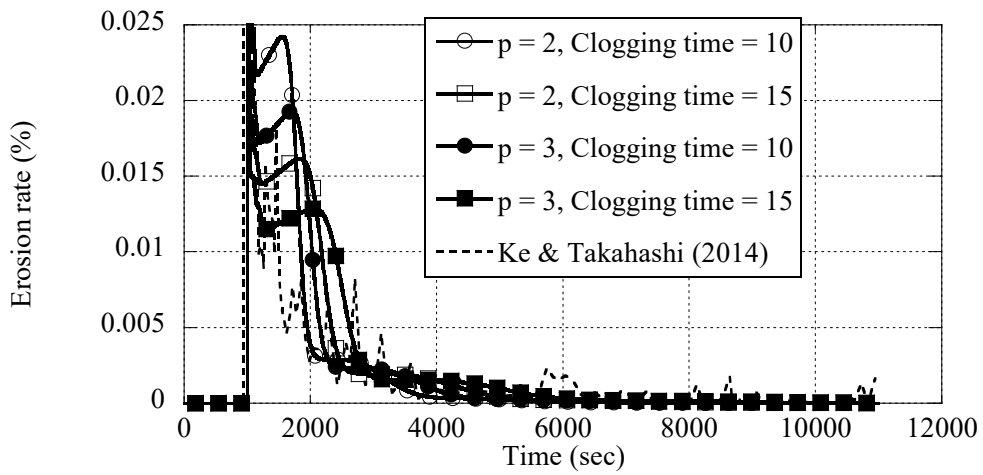
Fig. 19. Erosion rate under adjusted flow condition
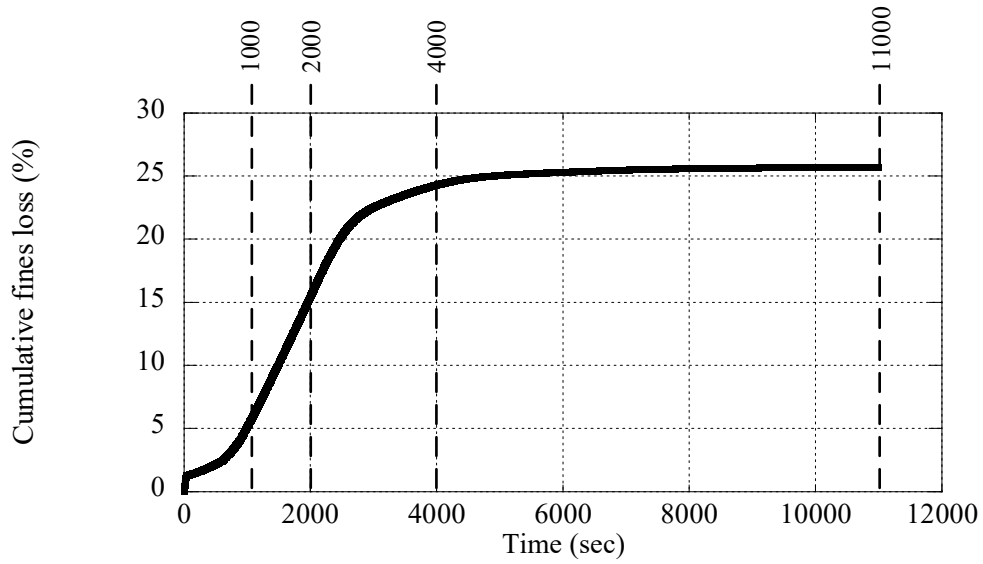
Fig. 20. Erosion curve under actual flow condition with $p = 2, \beta_{clog} = 15$

Fig. 21. Grain size distribution under actual flow condition

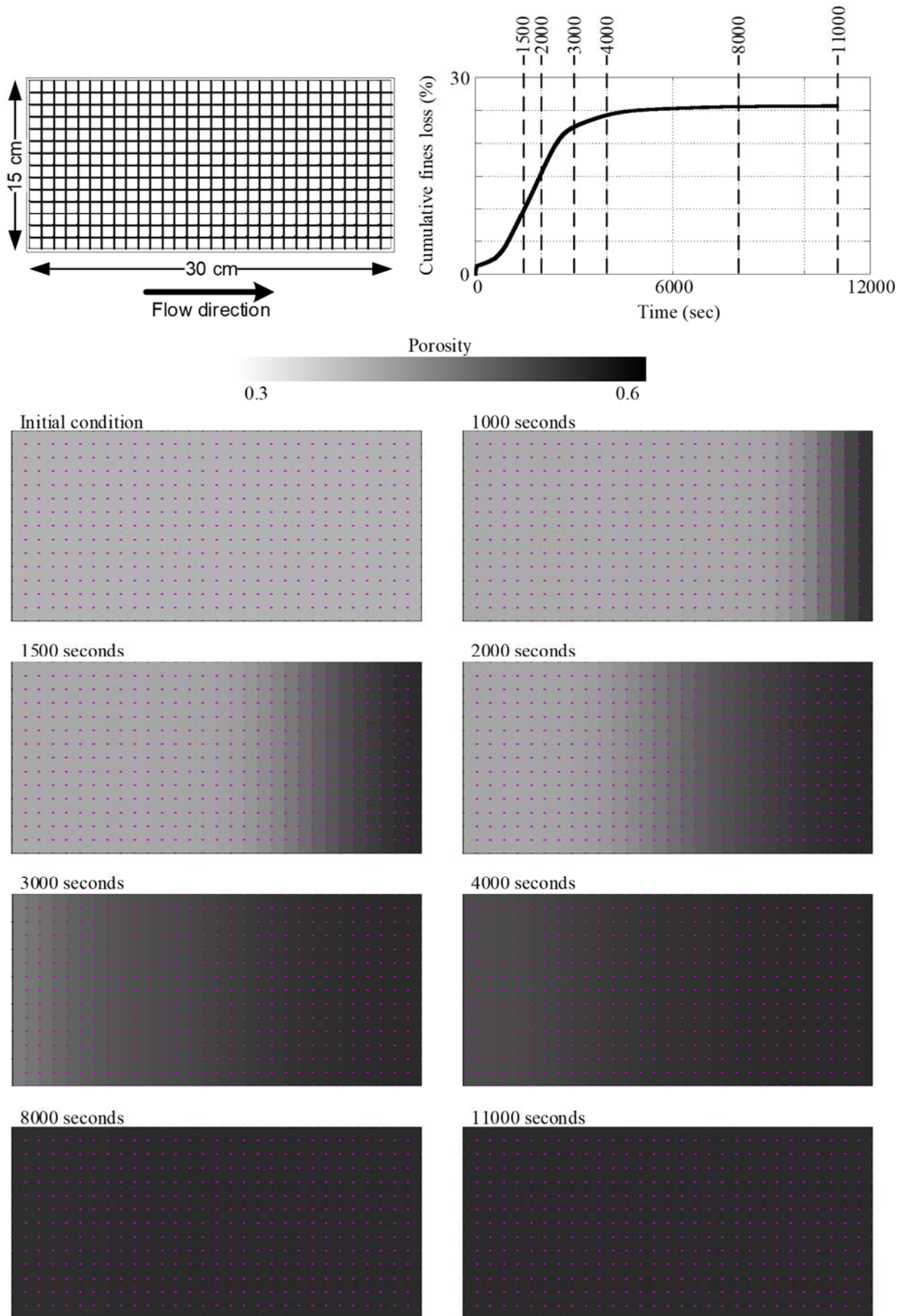**Fig. 22**. Cumulative curve for each grain size under actual flow condition
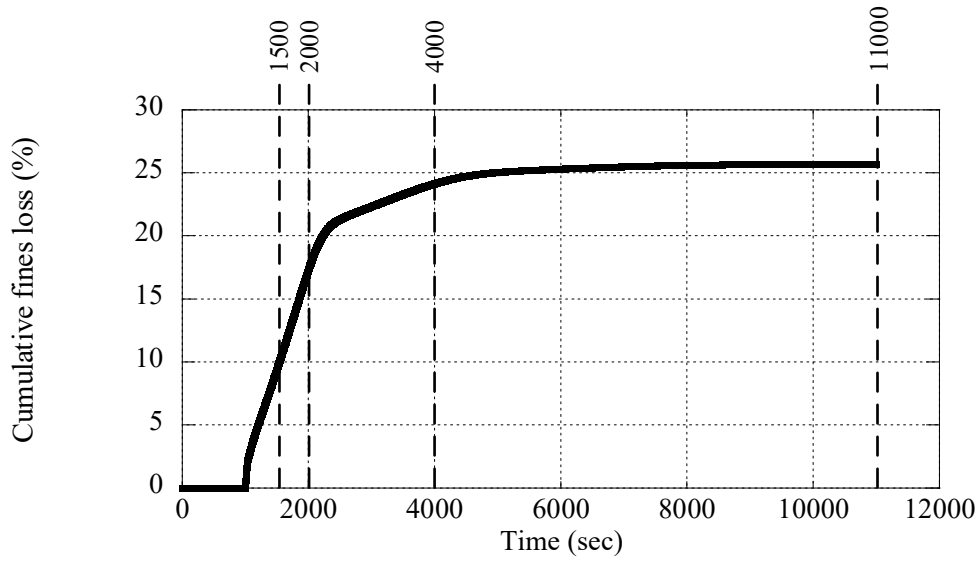
Fig. 23. Porosity contour under actual flow condition

Fig. 24. Erosion curve under adjusted flow condition with $p = 2, \beta_{clog} = 15$
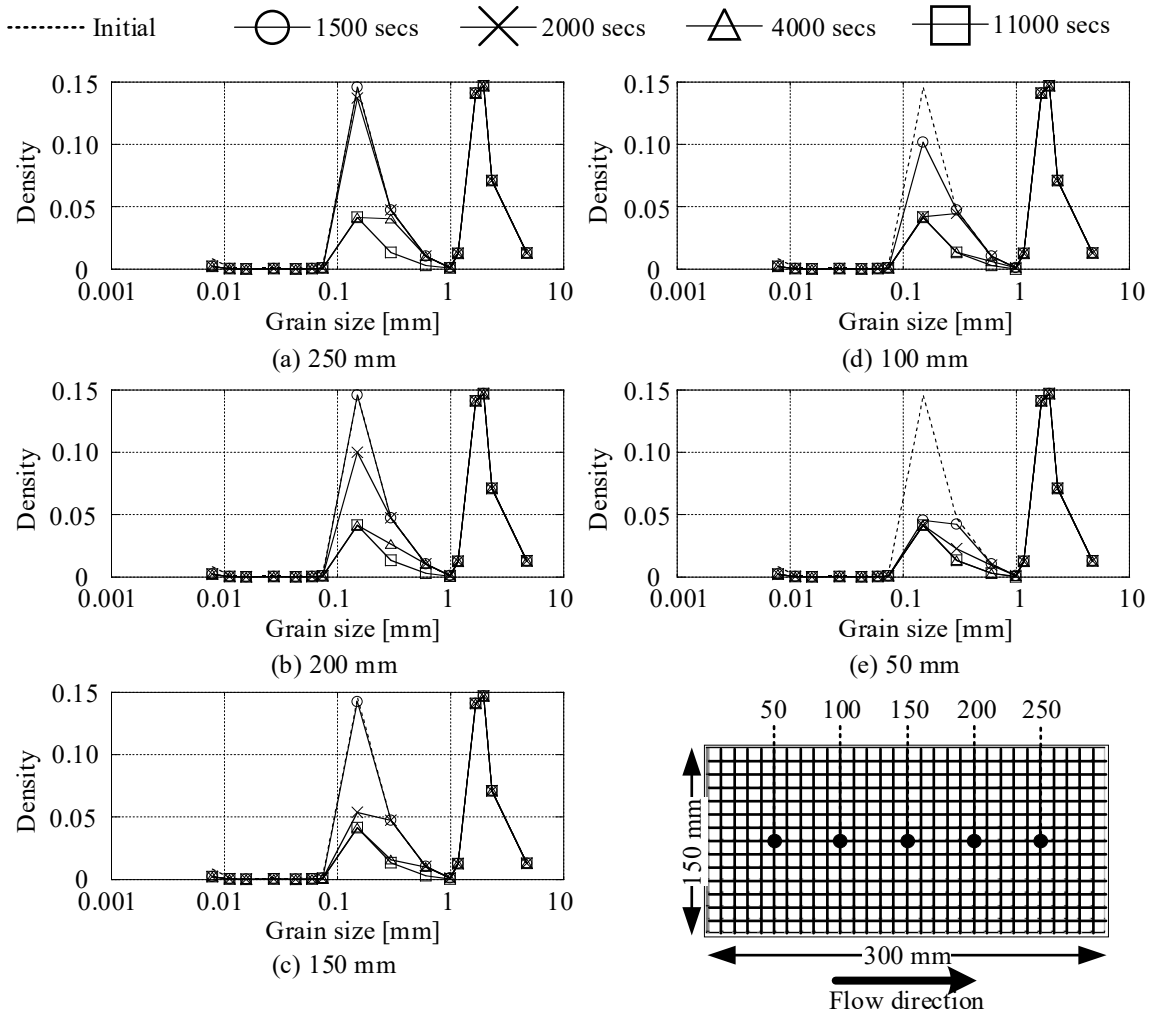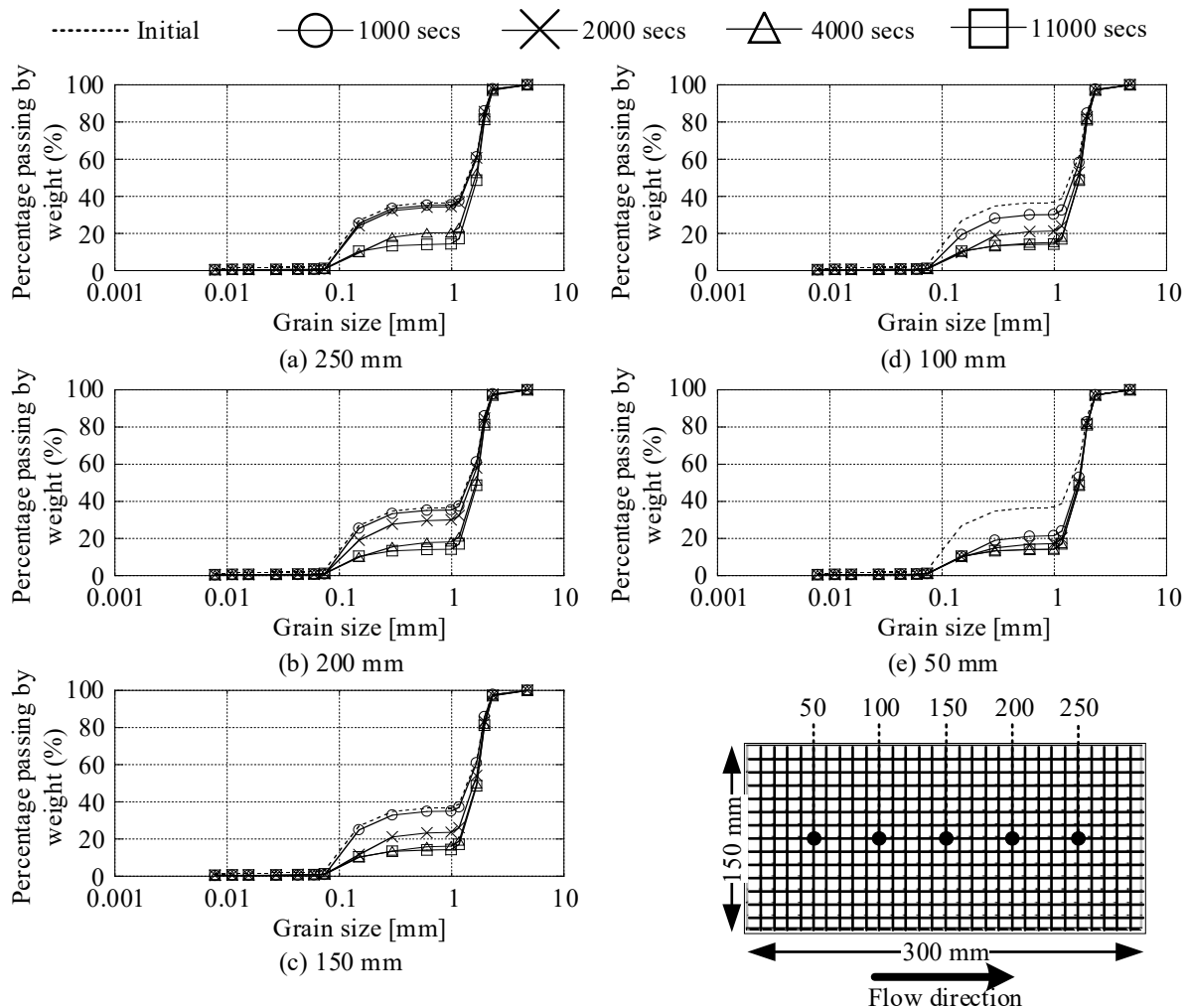

Fig. 25. Grain size distribution under adjusted flow condition

Fig. 26. Cumulative curve of grain size under adjusted flow condition

In addition, the cumulative fines loss for each particle size is depicted in **Fig. 28** to confirm that the erosion rate of the smaller particles tends to be faster than that of the larger particles. An example of separation during the cumulative fines loss was taken from the case in which the $p - value$ equals 2 under the adjusted fluid flow condition. The simulation results show that, for the small erodible particles, which are smaller than 0.1 mm in size, the slope of the cumulative fines loss is very steep. Furthermore, the large particles comprise a larger portion of the soil mass, being 0.9883, 0.2963, and 0.1494 mm in diameter, and take a longer time to become fully eroded. Conversely, the erodible particles comprise a smaller portion of the soil mass and become fully eroded starting at the beginning of the calculation.
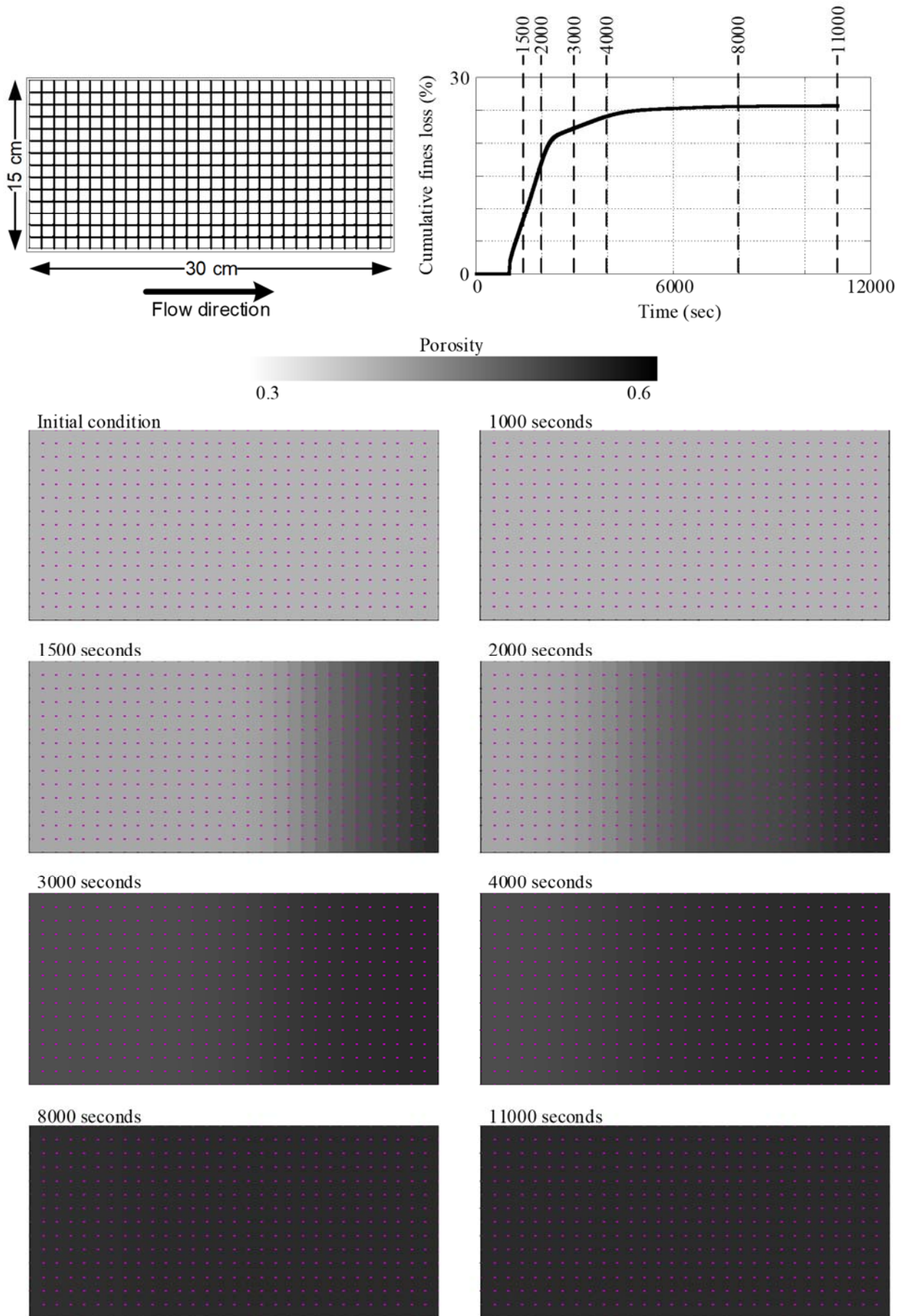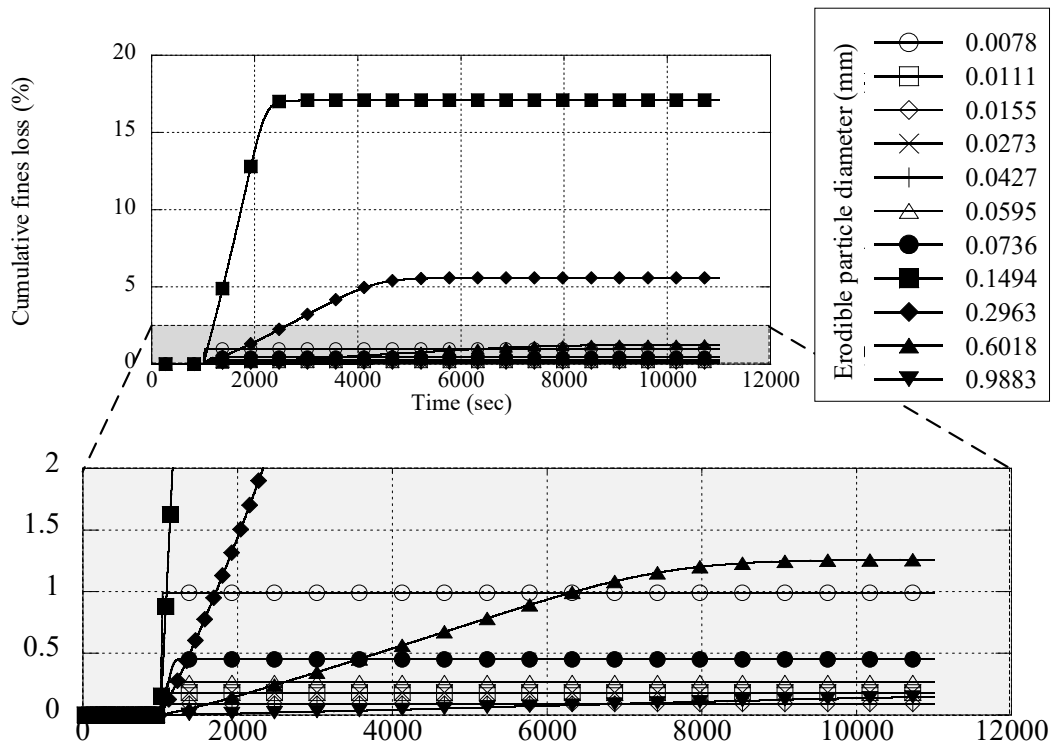
Fig. 27. Porosity under adjusted flow condition

Fig. 28. Cumulative fines loss of each particle size ($p = 2$)

Finally, a comparison of the experimental results and the numerical calculation under the adjusted flow condition will be shown again with different soil mixtures, following the report by Ke and Takahashi (2014). The numerical simulations which are used for a comparison with the experimental results were obtained from two different $p - values$. The lower bound and the upper bound for the $p - value$ of the soil material were assigned in the simulation and are shown in **Figs. 29** and **30**, respectively. According to the results, when the $p - value$ is equal to 3, it represents the tortuosity in very fine or clay material. Conversely, a lower $p - value$ stands for coarser material which is similar to the material used in the experiment (silica sand), but the simulation results show a greater difference. Furthermore, among the three different fines contents of 15%, 25% and 35%, the fines content from the numerical calculation shows more promise than that from the experiment for the fines content of about 25%.
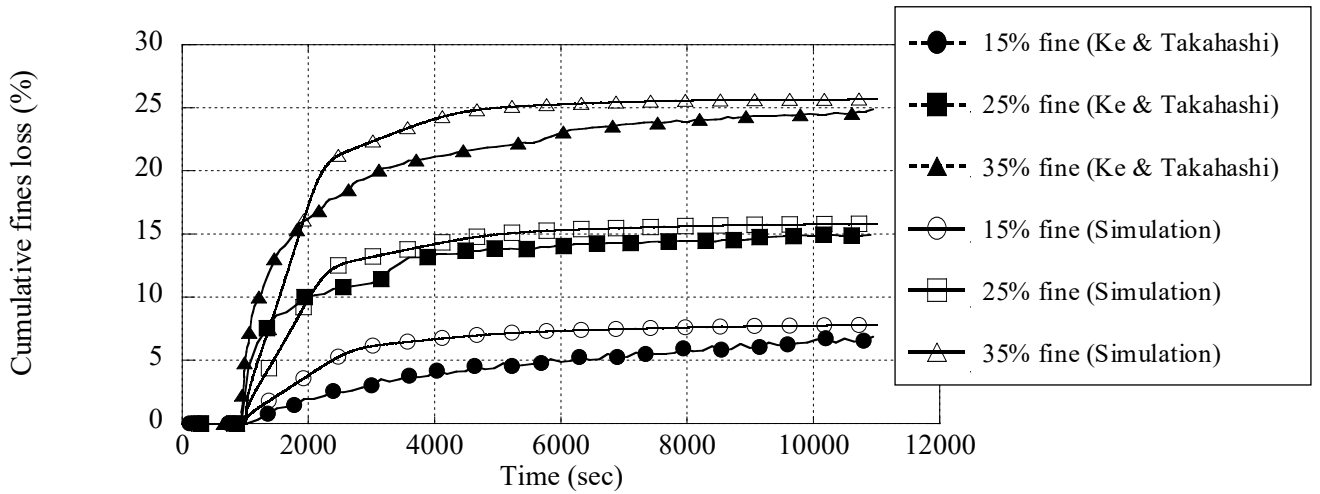
Fig. 29. Comparison of cumulative fines loss between experiment and simulation ($p = 2$)
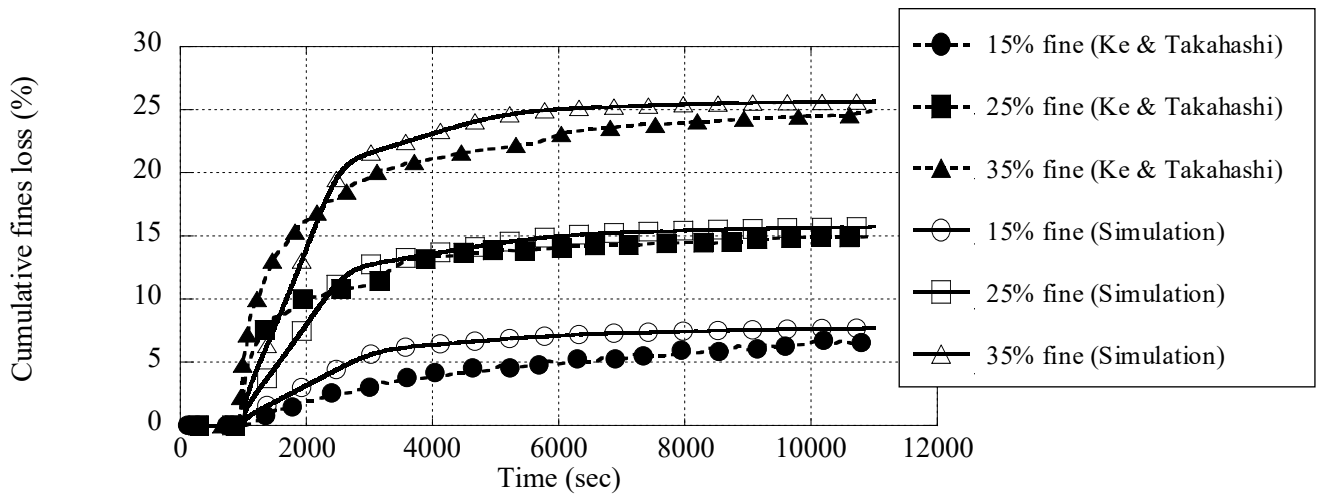
Fig. 30. Comparison of cumulative fines loss between experiment and simulation ($p = 3$)

Conclusion

The main purpose of this paper was to validate a new erosion model by conducting an investigation based on the previous experimental data from Ke and Takahashi (2014) collected under a constant fluid flow velocity. Hence, the present experimental data are quite beneficial for use in validating the erosion/suffusion modelling. The only data which were shown in the experiment were the cumulative fines loss. Therefore, the primary simulation output should be the cumulative fines loss as well. In addition, the data available from the previous experiment by Ke and Takahashi (2014)

included three different soil mixtures made of silica sand No. 3 and No. 8 to represent fine grain and coarse grain, respectively. In addition, the report from the previous experiment also mentioned that erosion is likely to start when the fluid flow reaches $1.34 \times 10^{-3} \, m/s$. Therefore, the numerical simulation was done under two different fluid flow conditions, namely, the actual flow and the adjusted flow, following the initiation of erosion.

The calculation, simulated under both the actual flow and the adjusted flow conditions, showed similar results in which the cumulative fines loss was slightly lower than that in the experiment at the beginning and then became higher than the experiment after 1500 to 2500 sec. Therefore, it can be implied that the erosion rate in the numerical simulation was lower than that in the experiment. However, the results of the simulation showed that the cumulative fines loss under the actual flow condition started earlier than that under the adjusted flow condition in accordance with the detachment of the fine erodible particles due to being under a low flow velocity.

The transport of the erodible particles in this simulation also showed the reduction in fine particles at each time and at each location of the soil sample. The fine particles at the downstream side were firstly washed out of the soil sample, particularly the particles of a small size.

However, the geo-material which was used in the experiment by Ke and Takahashi (2014) is a natural material which might influence the consistency of the results, due the material's heterogeneous properties. Especially in terms of particle geometry, a parametric study was done in this research on the variation in the clogging relaxation time and the $p-value$ in order to show the range in simulation results. Tortuosity is one of the main considerations in this simulation scheme; the tortuosity function requires the $p-value$. According to the previous study, a suitable $p-value$ for the soil material falls in the range of 2 and 3, while that recommended for sand or coarser grains is 2 and that for finer material or clay is 3. In addition, a higher $p-value$ represents a longer path inside the porous media. A comparison between the experiment by Ke and Takahashi (2014) and this simulation showed that a higher value for p provides more promising results than the experiment.

Finally, a comparison between the experiment data and the numerical simulation with three soil mixtures presented a good correlation between the experiment and the simulation when the fines content was about 25%. Nevertheless, the cumulative fines losses of the other two cases, of 15% and 35%, still differ slightly from that of the experiment, especially at the beginning of erosion. The simulation scheme in this paper still does not consider the stress effect which might be associated with the initiation of erosion and the active fines content or the residual fines content in the soil mass. Therefore, the stress and active fines content ratio will be necessary for realizing an erosion scheme which might be experimentally or analytically obtained.

Nomenclature

$\dot{\varepsilon}$	Erosion rate	α	Particle phase fraction
ω	Erosion coefficient	K_1, K_2	Coefficients in multiplier drag force coefficient equation
τ_a	Hydraulic shear stress	μ_f	Dynamic viscosity of fluid
τ_c	Critical hydraulic shear stress	$\mathbf{F_D^i}$	Drag force on particle group i index
φ_i	Concentration of erodible particles of group i index	C_D^i	Drag coefficient for particle group i index
φ_i^t	Concentration of fine particles of group i index	Re	Reynolds number
t	Time	m^i	Mass of particles in group i index
$\mathbf{u_e^i}$	Vector of particle flow velocity of particles of group i	$\emptyset$	Porosity
S_φ	Source term	$\mathbf{u_0}$	Average flow velocity or Darcy flow velocity
V_T	Total volume of soil mass at initial	p	Constant value for tortuosity calculation
V_e	Total volume of erodible soil	T	Tortuosity
V_s	Volume of soil skeleton	dl_0	Element size
V_{void}	Volume of void	τ, stk	Stokes number
V_e^i	Volume of erodible soil in group i index	T_a	Arrest time lapse
ρ_f	Density of fluid	β_{clog}	Clogging relaxation time (Stopping time)
ρ_s	Density of particles	t_p	Particle relaxation time (Stopping time)
C_D^i	Drag force coefficient of particles in group i index	t_{flow}	Characteristic time of fluid flow
d_e^i	Diameter of particle group i index	η	Solid-to-fluid density ratio
$\boldsymbol{u_f}$	Vector of intrinsic fluid flow velocity		
$\mathbf{u_0}$	Vector of Darcy flow velocity (fluid)		

References

1. Foster M, Fell R, Spannagle M. The statistics of embankment dam failures and accidents. *Canadian Geotechnical Journal*. 2000; 37(5):1000-1024. doi:10.1139/cgj-37-5-1000

2. Richards KS, Reddy KR. Critical appraisal of piping phenomena in earth dams. *Bulletin of Engineering Geology and the Environment*. 2007; 66(4):381-402. doi:10.1007/s10064-007-0095-0

3. Lane EW. Security from under-seepage-masonry dams on earth foundations. *Transactions of the American Society of Civil Engineers*. 1935; 100(1):1235-1272. doi:10.1061/taceat.0004655

4. Gabriella M. *Internal Erosion in the Pervious Foundation of an Embankment Dam: A Case Study of the Lossen Dam.*; 2016:3-5.

5. Bonelli S. *Erosion in Geomechanics Applied to Dams and Levees*. Wiley; 2013:2-83.

6. Robbins BA, Griffiths DV. Internal erosion of embankments: A review and appraisal. In: *Rocky Mountain Geo-Conference*. ASCE; 2018.

7. Telkar SG, Pote NS. Soil Erosion: Types and their mechanism. *Biomolecule Reports- An International eNewsletter*. 2018; (ISSN:2456-8759).

8. Tomlinson SS, Vaid YP. Seepage forces and confining pressure effects on piping erosion. *Canadian Geotechnical Journal*. 2000; 37(1):1-13. doi:10.1139/t99-116

9. Liang Y, Yeh T-CJ, Chen Q, Xu W, Dang X, Hao Y. Particle erosion in suffusion under isotropic and anisotropic stress states. *Soils and Foundations*. 2019; 59(5):1371-1384. doi:10.1016/j.sandf.2019.06.009

10. Bendahmane F, Marot D, Alexis A. experimental parametric study of suffusion and backward erosion. *Journal of Geotechnical and Geoenvironmental Engineering*. 2008; 134(1):57-67. doi:10.1061/(asce)1090-0241(2008)134:1(57)

11. Chang DS, Zhang LM. Critical hydraulic gradients of internal erosion under complex stress states. *Journal of Geotechnical and Geoenvironmental Engineering*. 2013; 139(9):1454-1467. doi:10.1061/(asce)gt.1943-5606.0000871

12. Fujisawa K, Murakami A, Nishimura S-I. Numerical analysis of the erosion and the transport of fine particles within soils leading to the piping phenomenon. *Soils and Foundations*. 2010; 50(4):471-482. doi:10.3208/sandf.50.471

13. Liang Y, Yeh T-CJ, Wang Y-L, Liu M, Wang J, Hao Y. Numerical simulation of backward erosion piping in heterogeneous fields. *Water Resources Research*. 2017; 53(4):3246-3261. doi:10.1002/2017wr020425

14. Arulanandan K, Krone RB, Loganathan P. Pore and eroding fluid influences on surface erosion on soil. *Journal of the Geotechnical Engineering Division*. 1975; 101(1):51-66. doi:10.1061/ajgeb6.0000141

15. Chaney R, Demars K, Reddi L, Lee I-M, Bonala M. Comparison of internal and surface erosion using flow pump tests on a sand-kaolinite mixture. *Geotechnical Testing Journal*. 2000; 23(1):116. doi:10.1520/gtj11129j

16. Kodieh A, Gelet R, Marot D, Fino AZ. A study of suffusion kinetics inspired from experimental data: comparison of three different approaches. Acta Geotechnica. 2020;16(2):347-365. doi:10.1007/s11440-020-01016-5

17. Khilar KC, Fogler HS, Gray DH. Model for piping - plugging in earthen structures. *Journal of Geotechnical Engineering*. 1985; 111(7):833-846. doi:10.1061/(asce)0733-9410(1985)111:7(833)

18. Fujisawa K, Murakami A, Nishimura S, Shuku T. Relation between seepage force and velocity of sand particles during sand boiling. *Geotechnical Engineering Journal of the SEAGS & AGSSEA*. 2013; 44(2):9-17.

19. Vardoulakis I, Stavropoulou M, Papanastasiou P. Hydro-mechanical aspects of the sand production problem. *Transport in Porous Media*. 1996; 22(2):225-244. doi:10.1007/bf01143517

20. Liu Y, Wang L, Hong Y, Zhao J, Yin Z. A coupled CFD-DEM investigation of suffusion of gap graded soil: Coupling effect of confining pressure and fines content. International Journal for Numerical and Analytical Methods in Geomechanics. 2020;44(18):2473-2500. doi:10.1002/nag.3151

21. Xiong H, Yin Z-Y, Zhao J, Yang Y. Investigating the effect of flow direction on suffusion and its impacts on gap-graded granular soils. Acta Geotechnica. 2020;16(2):399-419. doi:10.1007/s11440-020-01012-9

22. Ma Q, Wautier A, Zhou W. Microscopic mechanism of particle detachment in granular materials subjected to suffusion in anisotropic stress states. Acta Geotechnica. 2021;16(8):2575-2591. doi:10.1007/s11440-021-01301-x

23. Yang J, Yin Z-Y, Laouafa F, Hicher P-Y. Hydromechanical modeling of granular soils considering internal erosion. *Canadian Geotechnical Journal*. 2020; 57(2):157-172. doi:10.1139/cgj-2018-0653

24. Russell EM. Particle Transport in Flow through Porous media: Advection, Longitudinal dispersion, and Filtration. Published online 1992.

25. Bear J. *Dynamics of Fluids in Porous Media*. Dover; 1988.

26. Koenders MA, Williams AF. Flow equations of particle fluid mixtures. *Acta Mechanica*. 1992; 92(1-4):91-116. doi:10.1007/bf01174169

27. Ke L, Ouyang M, Horikoshi K, Takahashi A. Soil deformation due to suffusion and its consequences on undrained behavior under various confining pressures. *Japanese Geotechnical Society Special Publication*. 2016; 2(8):368-373. doi:10.3208/jgssp.jpn-083

28. Mehdizadeh A, Disfani MM, Shire T. Post-erosion mechanical response of internally unstable soil of varying size and flow regime. *Canadian Geotechnical Journal*. 2021; 58(4):531-539. doi:10.1139/cgj-2019-0790

29. Snorri Gudmundsson. *General Aviation Aircraft Design*. Elsevier - Health Sciences Division; 2014.

30. Boiko VM, Pivovarov AA, Poplavski SV. Measurement of gas velocity in a high-gradient flow, based on velocity of tracer particles. *Combustion, Explosion, and Shock Waves*. 2013; 49(5):548-554. doi:10.1134/s0010508213050067

31. Morsi SA, Alexander AJ. An investigation of particle trajectories in two-phase flow systems. *Journal of Fluid Mechanics*. 1972; 55(02):193. doi:10.1017/s0022112072001806

32. Davuluri RSC, Bailey SCC, Tagavi KA, Martin A. A drag coefficient model for Lagrangian particle dynamics relevant to high-speed flows. *International Journal of Heat and Fluid Flow*. 2021; 87:108706. doi:10.1016/j.ijheatfluidflow.2020.108706

33. Chadil M-A, Vincent S, Estivalèzes J-L. Accurate estimate of drag forces using particle-resolved direct numerical simulations. *Acta Mechanica*. 2018; 230(2):569-595. doi:10.1007/s00707-018-2305-1

34. Dioguardi F, Mele D, Dellino P. A new one-equation model of fluid drag for irregularly shaped particles valid over a wide range of Reynolds number. Journal of Geophysical Research: Solid Earth. 2018;123(1):144-156. doi:10.1002/2017jb014926

35. Ke L, Takahashi A. Experimental investigations on suffusion characteristics and its mechanical consequences on saturated cohesionless soil. *Soils and Foundations*. 2014; 54(4):713-730. doi:10.1016/j.sandf.2014.06.024

36. Barnea E, Mizrahi J. A generalized approach to the fluid dynamics of particulate systems. *The Chemical Engineering Journal*. 1973; 5(2):171-189. doi:10.1016/0300-9467(73)80008-5

37. Rusche H, Issa R. The effect of voidage on the drag force on particles in dispersed two-phase flow. Published online 2000.

38. Perry RH, Cecil Hamilton Chilton, John Howard Perry. *Chemical Engineers' Handbook. 5th Ed. Prepared by a Staff of Specialists, under the Editorial Direction of Robert H. Perry [And] Cecil H. Chilton.* New York McGraw-Hill; 1973.

39. Flemmer RLC, Banks CL. On the drag coefficient of a sphere. *Powder Technology*. 1986; 48(3):217-221. doi:10.1016/0032-5910(86)80044-4

40. Haider A, Levenspiel O. Drag coefficient and terminal velocity of spherical and nonspherical particles. *Powder Technology*. 1989; 58(1):63-70. doi:10.1016/0032-5910(89)80008-7

41. Turton R, Levenspiel O. A short note on the drag correlation for spheres. *Powder Technology*. 1986; 47(1):83-86. doi:10.1016/0032-5910(86)80012-2

42. Fanchi JR. *Shared Earth Modeling*. Butterworth-Heinemann; 2002.

43. Faruk Civan. *Reservoir Formation Damage: Fundamentals, Modeling, Assessment, and Mitigation*. Elsevier Ltd; 2016.

44. Matyka M, Khalili A, Koza Z. Tortuosity-porosity relation in porous media flow. *Physical Review E*. 2008; 78(2). doi:10.1103/physreve.78.026306

45. Comiti J, Renaud M. A new model for determining mean structure parameters of fixed beds from pressure drop measurements: application to beds packed with parallelepipedal particles. *Chemical Engineering Science*. 1989; 44(7):1539-1545. doi:10.1016/0009-2509(89)80031-4

46. Barrande M, Bouchet R, Denoyel R. Tortuosity of porous particles. *Analytical Chemistry*. 2007; 79(23):9115-9121. doi:10.1021/ac071377r

47. Boudreau BP, Meysman FJR. Predicted tortuosity of muds. *Geology*. 2006; 34(8):693. doi:10.1130/g22771.1

48. Iversen N, Jørgensen BB. Diffusion coefficients of sulfate and methane in marine sediments: Influence of porosity. *Geochimica et Cosmochimica Acta*. 1993; 57(3):571-578. doi:10.1016/0016-7037(93)90368-7

49. Israel R, Rosner DE. Use of a generalized Stokes number to determine the aerodynamic capture efficiency of non-Stokesian particles from a compressible gas flow. *Aerosol Science and Technology*. 1982; 2(1):45-51. doi:10.1080/02786828308958612

50. Liu Q, Zhao B, Santamarina JC. Particle migration and clogging in porous media: a convergent flow microfluidics study. *Journal of Geophysical Research: Solid Earth*. 2019; 124(9):9495-9504. doi:10.1029/2019jb017813

51. Koch DL, Hill RJ. Inertial effects in suspension and porous media flows. *Annual Review of Fluid Mechanics*. 2001; 33(1):619-647. doi:10.1146/annurev.fluid.33.1.619

52. Brandon DJ, Aggarwal SK. A numerical investigation of particle deposition on a square cylinder placed in a channel flow. *Aerosol Science and Technology*. 2001; 34(4):340-352. doi:10.1080/02786820121279

53. Aidun CK, Lu Y, Dian E-J. Direct analysis of particulate suspensions with inertia using the discrete Boltzmann equation. *Journal of Fluid Mechanics*. 1998; 373:287-311. doi:10.1017/s0022112098002493

54. Souzy M, Zuriguel I, Marin A. Transition from clogging to continuous flow in constricted particle suspensions. *Physical Review E*. 2020; 101(6). doi:10.1103/physreve.101.060901

55. Zuriguel I, Parisi DR, Hidalgo RC, et al. Clogging transition of many-particle systems flowing through bottlenecks. *Scientific Reports*. 2014; 4(1). doi:10.1038/srep07324